FABRICATION OF ELASTOMER/METAL BILAYERS USING STRAIN ENGINEERING

A Thesis
Presented to
The Academic Faculty

by

Timothy Ibru

In Partial Fulfillment
of the Requirements for the Degree
Master of Science in Mechanical Engineering in the
School of Mechanical Engineering

Georgia Institute of Technology
May 2017

FABRICATION OF ELASTOMER/METAL BILAYERS USING STRAIN ENGINEERING

Approved by:

Dr. Antonia Antoniou, Advisor
School of Mechanical Engineering
Georgia Institute of Technology

Dr. Kyriaki Kalaitzidou
School of Mechanical Engineering
Georgia Institute of Technology

Dr. Karl I. Jacob
School of Material Science and Engineering
Georgia Institute of Technology

Date Approved: Thursday, March 16, 2017

ACKNOWLEDGEMENTS

I would like to express my sincere gratitude to everyone that assisted me over the course of this program. Primarily, I would like to thank Professor Antonia Antoniou and Professor Kyriaki Kalaitzidou for giving me the opportunity to work on this project, for their confidence in my ability, their patience and understanding during the times when I struggled and tried to adapt to the graduate pace of life, and for their unwavering optimism even when it seemed like success was impossible. I am extremely grateful for the academic as well as life lessons that I have learned from them over the course of this project. I would also like to thank the students and faculty that provided advice and support in this project, including Ran Liu and Tamanna Rahman, who helped answer my most trivial questions, the IEN staff, Eric Woods, Walter Henderson, and Todd Walters, who were available to answer my technical questions and present invaluable advice and suggestions as I tried to navigate the IEN and operate the facilities, and the student services office of the Mechanical Engineering Department, for guiding me through complicated logistics of the graduate school system. I would also like to express my gratitude to the thesis committee and Dr. Karl Jacob for agreeing to take time to participate in the committee even though there have been many uncertainties along the way. Finally, I would like to thank friends and family that walked with me through the journey, supporting me through periods of high discouragement and for challenging me to keep trying and praying, constantly reminding me of the bigger picture of life beyond the failures and disappointments of research and other academic struggles.

TABLE OF CONTENTS

LIST OF FIGURES

LIST OF TABLES

SUMMARY

Bilayers are constructed from two materials with distinct properties and one physical dimension one order of magnitude smaller than others. Due to the property mismatch, dimensional changes in each material will be different when the bilayer is exposed to different environments. This can result in out-of-plane deformation in the bilayer as a way to minimize its potential energy. The resulting curvature change is dependent on the environment and can be tuned by altering the material elastic properties and relative thicknesses. At the same time, it is possible to initiate other instabilities or defects during the fabrication process when mismatch strains develop that can influence the eventual curvature of the bilayer. Existing analyses predict that surface instabilities, such as wrinkles, folds, and creases, form in large property mismatched bilayers and become more prominent with increased compressive mismatch strains locked at the interface. Under compressive stress, cracks have been assumed to form only when the interfacial strength is weak, allowing the film to detach from the substrate.

The aim of this work is to describe the synthesis parameters for bilayers formed when thin metal alloy films sputter deposited on compliant substrates. Specifically, we consider metal alloy films sputter deposited under bias on elastomers of different thickness, curing temperature or surface treatment. The deposition parameters created residual compressive strains and strong adhesion in the bilayers. After deposition, nested wrinkles formed at the surface of some of the samples with smaller wavelengths than theoretical predictions. Contrary to conventional expectations, the experiments revealed that cracks could form on surfaces under compressive mismatch strain when the interface is strong. The crack spacing was found to decrease by a factor of four when the surface was UV treated and a factor of three as elastomer thickness decreased from 30 to $6\mu m$. Cracks penetrated through the elastomer and formed in all samples with brittle coating. Crack depth was two orders of magnitude greater than the film thickness. A numerical model was developed to explain

the formation of cracks in the presence of compressive mismatch strains. The model showed nested wrinkles formed when the mismatch strain profile penetrated 100 nm into the elastomer and had comparable wavelength as observed in the experiments. The model suggests that cracks can initiate from the peak of wrinkles when the critical fracture strength of the coating is exceeded.

The work impacts design of bilayers with extreme property mismatches since the fracture toughness of the film may be low enough to initiate cracks and possibly compromise formation of any desired instabilities e.g. wrinkles or folds. Therefore, phase diagrams predicting complex surface instabilities, e.g. folds, may not be feasible for all material systems. Furthermore, the particular metal alloys used in this work can be further etched to form nanoporous metal on the elastomer surface. Nanoporous metals have high surface to volume ratios, high strength and moderate stiffness when compared to their fully dense counterparts. Formation of wrinkles or cracks in the precursor thin metal alloy may affect the dealloying and eventual formation of the nanoporous network.

CHAPTER 1

INTRODUCTION

1.1 Strain Engineered Multi- and Bilayers

Strain engineering uses mismatch strains developed at the interface of planar hetero-structures consisting of two or more dissimilar materials e.g. bi or multilayers to elicit a desired response, or fabricate complex shapes. The overall layer physical dimensions range from the nanoscale to the macroscale with one of the physical dimensions being at least an order of magnitude smaller than other dimensions. The release of the residual stresses causes bending/folding of the planar heterostructure leading to 3D structures. The process, driven by self-assembly is simple, robust, scalable and versatile because it is applicable to a wide range of material combinations, as long as the materials used to form the planar heterostructure have a significant difference in a given property and strong adhesion at their interface. Oftentimes, the excess potential energy of the system may be alleviated by formation of defects e.g. cracks or instabilities that may limit the functionality or eventual out of plane deformation of the structure. Depending on the application, such defects or instabilities may be desired or unavoidable.

In the microelectronics field, for instance, bi or multilayers of conducting and insulating materials in the micron and nano- scale are commonly used in the assembly of integrated circuits. In particular, the design of flexible electronics poses additional challenges since there can be vast property mismatches between the compliant and bendable substrate and the conductive components. Mismatch strains during fabrication are locked at the interface and residual stress build up can be relieved by various mechanisms including wrinkle[1-5] or crack formation[6]. Excessive buildup of mismatch strains due to large property mismatches of the layers may lead to circuit failures [7-10].

Mismatch strains can also develop in freestanding layers of dissimilar materials when there is a change in the environment e.g. due to chemical, electrical, thermal fields that elicit a different change in the physical dimensions of each layer. Because of the disparate dimensional changes, the multilayer curvature may change. The layer may reversibly return to its original shape when the environmental stimulus is removed. This is the principle behind the design of thermostats [7, 11, 12] but there are several other applications including more recently in the fabrication of three-dimensional micro-/nano-objects [13-16] including capacitors, building blocks for transistors, sensors and MEMS [13, 17] that exploit the difference in properties to create self-assembled structures of various intricate shapes.

1.2 Motivation and Description of the Performed Work

Regardless of the motive for creating such bi or multilayers, a reliable fabrication route is needed that takes into consideration the buildup of strains and addresses any instabilities or defects that may form as a result.

The work is aimed at specifically addressing

1) What type of instabilities or defects develop in bilayers with extreme modulus mismatch and strong interfacial adhesion? Although several guidelines in design have been well documented [6, 18], the current body of work suggests that instabilities that may form with excessive compressive strain are only limited by interfacial delamination. This work specifically examines patterns that form on the surface of metal alloy or metal silicon alloy nano-sized coatings that are sputter deposited on elastomeric substrates, e.g. polydimethylsiloxane (PDMS), with micron scale thickness. PDMS and metal alloy coating are at the extreme Dundurs' parameter range of $D_1 = 1$ and $D_2 \sim 0$ [19] where the Dundurs' parameters define interrelations between thin film coating and substrate elastic properties[19].

2) What processing parameters control the presence of the aforementioned instabilities or defects?

Such an understanding can have a two-fold impact: i) provide the optimum processing window for such structures so that the maximum possible stresses can be locked at the interface while avoiding excessive damage and ii) provide guidelines on how to intentionally create defects or instabilities in a controlled way. As a final demonstration, the thesis will provide recommendations on dealloying protocols for synthesis of nanoporous metals on compliant substrates.

1.3 Background

1.3.1 Applications for bilayer heterostructures

In the most basic and common form, the soft-metallic bilayers that we discuss in this thesis could serve as actuators. The bimetallic strip is a well-known example. In addition, several studies have demonstrated this actuation behavior. For instance, in Figure 1.1, Kalaitzidou et al. [20] show the reversible bending of bilayers of similar configuration to those discussed in this thesis. These are shown to actuate using a thermal stimulus: In the figure, (a) shows the folding and unfolding of polymer scrolls upon temperature change while (b) illustrates the alignment of the rolled structures along a flow field, as would be essential in practical applications. The design of these actuators requires a deep understanding of crucial fabrication factors. For example, the amount of bending is dependent on the level of intrinsic stresses expected. In addition, reducing the number of flaws in the generated samples requires maintaining intrinsic residual stresses at a minimum.

The reversible bending property of these Au/PDMS bilayers, as well as other bilayers with a similar configuration, could serve the tangible application of capture, transport and release processes. During these processes, molecules are captured by

adsorption or a similar means, transported and then released, by desorption, in a desired location. In the example demonstrated by Simpson et.al [21], the bilayers are used to transport poly(ethylene glycol) (PEG), which is more easily adsorbed onto the flat surface of the bilayers compared to the folded bilayers. Taking advantage of this selective adsorption, the researchers heated initially rolled bilayers in a solution to facilitate unfolding, and then exposed these flat bilayers to PEG. The PEG was readily adsorbed onto this unfolded surface, after which the bilayers were cooled in the solution, rolling into tubes once again, and transported to a separate location. The aspect ratio of the rolled tubes supported transportation in a flow field to the new location, where the tubes were once again heated to unroll and release the PEG by desorption.

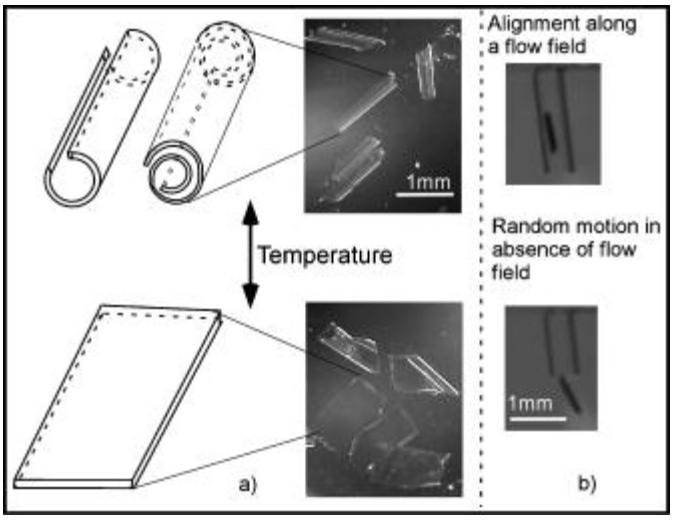

Figure 1.1: Bilayer actuation under thermal stimulus. [20]

Bilayers also actuate under other stimuli, besides the commonly applied thermal stimulus [22, 23]. An example of a bilayer actuator that uses a non-thermal stimulus for actuation has been demonstrated by Dai et al. [22]. These researchers created bilayers of a liquid crystalline (LC) polymer and the polymer polyamide-6 (PA-6): A flexible polymer, PA-6 has been used in a number of applications [24, 25]. Although they used the PA-6 polymer, theoretically, any other polymer that adheres properly to the LC polymer and that

can withstand the processing steps would suffice. Once activated in NaOH, the LC polymer undergoes anisotropic expansion in a high relative humidity environment. PA-6, by contrast, does not exhibit this behavior, so when both layers are bonded and placed in a high humidity environment, the LC polymer expands at the expense of the PA-6, resulting in a bending motion similar to that of thermal responsive bilayers.

The possibility of actuation under a wide range of stimuli creates potential for these bilayers to be applied to sensor designs. The aforementioned bilayer configuration, for instance, which actuates under changes in relative humidity, could be incorporated into a design that detects humidity in an environment. Similarly, bilayers that actuate by thermal or other stimuli could similarly be applied to detect environmental changes in the properties that stimulate their actuation. Ultimately, regardless of the general approach used, be it thermal or otherwise, actuation requires strong adhesion and a property mismatch that leads to differential thermal deformation under specific stimuli. In order to design a successful actuation event/procedure, or to understand the limitations of such a design, researchers must have a deep understanding of crucial fabrication factors for developing an ideal structure. Intrinsic residual stresses, for instance, would have to be kept at a minimum to reduce flaws in the generated samples. The goal of this thesis is to reinforce the knowledge base associated with bilayer fabrication challenges with findings from our studies.

1.3.2 Micro Fabrication for Bilayer Actuation

A primary application, for micro-scale bilayers is in the field of micro and nanofabrication, which typically requires unique development approaches because conventional techniques become less feasible below the micro-/nano- size threshold: As no single overarching technique is ideal for developing every micro- and nano- feature, we can use several specific development approaches to create desired features. However, because most techniques have strict constraints and design limitations, not all development approaches are appropriate for certain applications. For instance, some structures

composed of organic materials such as polymers are often incompatible with the most versatile techniques such as lithography and ion beam or X-ray milling. Thus, as they can be applied in alternative development techniques, the bilayer structures discussed in this thesis are essential.

The actuation approach has been applied in the fabrication of three-dimensional structures [20, 26]. These structures could serve applications in a wide range of micro- and nano-scale systems such as microelectromechanical systems (MEMS), microchemomechanical systems (MCMS), and nanoelectromechanical systems (NEMS) [23, 27, 28]. At the core of the technique is the bilayer and the property differences that facilitate the fabrication processes. The general approach is to bend sheets of film in unique ways that result in desired structures. The most common and easiest application is in the development of tubes, coils, arcs, and drills, which require a bilayer under either intrinsic stresses, such as those introduced during the fabrication process, or by external stimuli, such as a temperature change that leads to the differential expansion of the layers.

1.3.3 "Defects" in Bilayers

Although counter intuitive, some designers wish to create crack surface patterns in bilayers. These could prove useful in applications such as the testing of fluid channels or the aiding of actuation. In addition to the common method, forming a basic arc structure, other methods can create a much more complex pattern. One such method is the kirigami-type structure. The method of forming this unique pattern involves strategically placing cuts on the manufactured bilayer and applying planar stresses, which may have been significantly more complicated to develop otherwise. The cuts direct bending in certain directions, as reported in the work of Zhang et al. and illustrated in Figure 1.2 [29].

A similar application uses cuts to guide the formation of cracks for unique applications. During this procedure, cracks generated by increased residual stresses can be tuned so that they occur in desired regions of a sample [30, 31]. An example of this is

shown in Figure 1.3, where Kim et al. [30] make use of notches to guide the propagation of cracks. In some cases, these guided cracks serve to create micro- and nano- channels [32-34], or they could aid actuation behavior in a manner similar to that of kirigami structures. While applying such methods, a designer, who would need more than an understanding of how to keep intrinsic stresses at a minimum, must be able to keep stresses within a confined range and understand the potential instabilities, a requirement that demands a deeper understanding of the fabrication steps and contributors to stress and crack formation.

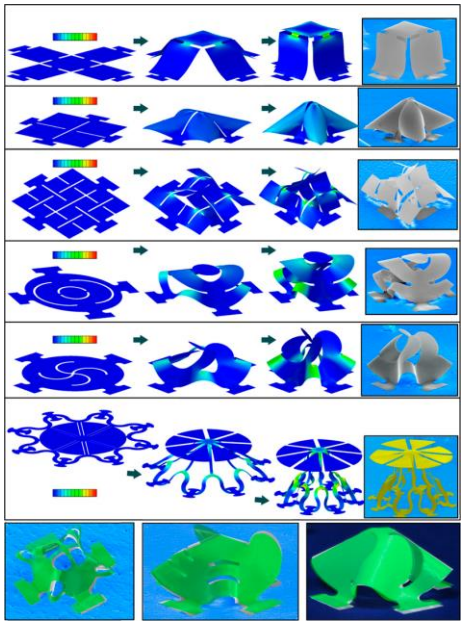

Figure 1.2: Illustration of the Kirigami application of bilayer structures [29]

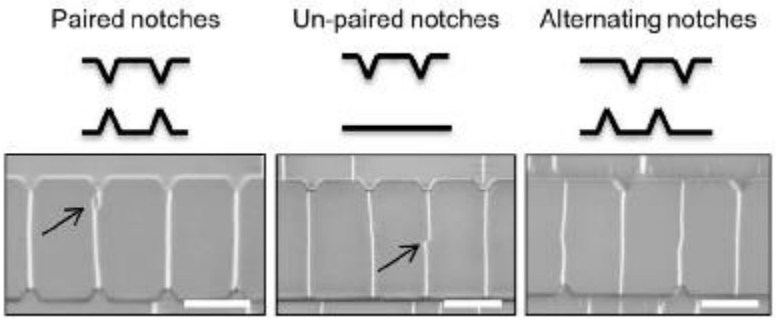

Figure 1.3: Example of Guided Crack Formation [30]

Several studies characterize the behavior of instabilities under various loading conditions and design configurations. One of the most concise of these studies was conducted by Wang et al. [35], who developed a three-dimensional phase diagram for surface instabilities as a function of the level of mismatch strain, the modulus mismatch, and the level of adhesion between the layers of the bilayer. The concise phase diagram is shown in Figure 1.4. However, this phase diagram does not accurately depict all possible behaviors; some of the results reported herein deviate from predictions from the chart. Hence, an objective of this study is to examine the unique situations observed and complement the information already available to describe the behavior of instabilities.

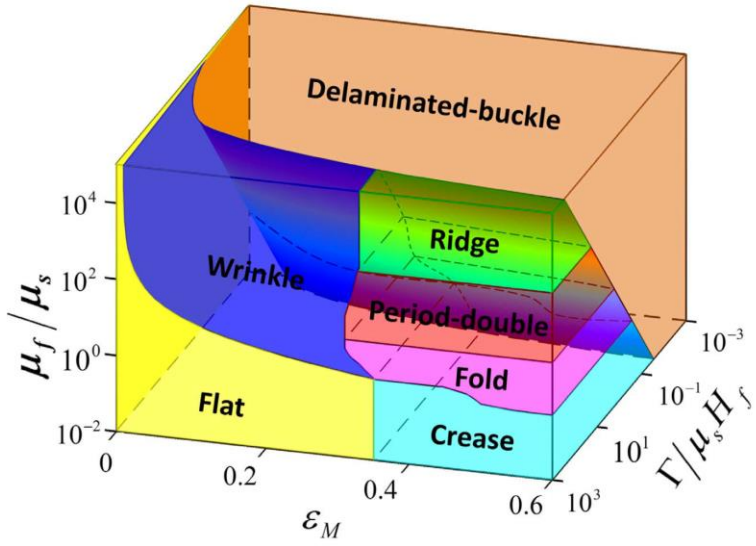

Figure 1.4: Phase Diagram of Surface Instabilities by Wang et al. [35]

1.3.4 Characterizing the Bilayer Configuration

The previous section introduces the idea of high mismatch bilayers and the challenges they present. However, to some degree, all bilayers consist of dissimilar materials. Quantifying this dissimilarity and the level of mismatch requires a metric. The most accepted quantifying tool is a set of equations developed by Dundurs [19, 36]. These so-called "Dundurs' parameters" relate the stiffness of the individual layers and gauges the

mismatch. The equations in their original nomenclature are expressed as Equations 1 and 2:

$$\alpha = \frac{k(\kappa_s+1)-(\kappa_f+1)}{k(\kappa_s+1)+(\kappa_f+1)} \tag{1}$$

$$\beta = \frac{k(\kappa_s-1)-(\kappa_f-1)}{k(\kappa_s+1)+(\kappa_f+1)} \tag{2}$$

where α and β are the first and second Dundurs' parameters, k the ratio of the shear moduli μ_f/μ_s, ν_i the Poisson ratio, and the Muskhelishwili constant $\kappa_i = (3-4\nu)$ for plane strain, and $(3-\nu_i)/(1+\nu_i)$ for plane stress [37]. Several other versions of the equations use distinct nomenclature that directly show the role of other parameters. Equations 3 and 4 represent a simplified form of the equations that shows the role of the moduli:

$$\alpha = \frac{\bar{E}_f-\bar{E}_s}{\bar{E}_f+\bar{E}_s} \tag{3}$$

$$\beta = \frac{\bar{E}_f f(\nu_s)-\bar{E}_s f(\nu_f)}{\bar{E}_f+\bar{E}_s} \tag{4}$$

Here, $\bar{E}$ represents the biaxial modulus given by $\bar{E} = E/(1-\nu^2)$ for plane strain and $\bar{E} = E$ for plane stress, and subscripts f and s refer to the film and substrate layers, respectively, as illustrated in Figure 1.5. A function of the Poisson ratio used in the second Dundurs' parameter is given as $f(\nu) = (1-2\nu)/[2(1-\nu)]$.

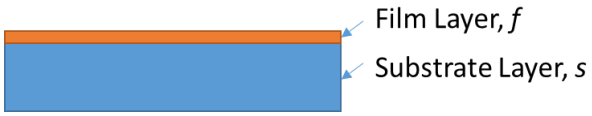

Figure 1.5: Schematic illustration of the bilayer configuration

The first Dundurs' parameter, α, is generally used for characterizing the relative stiffness of the two layers while the second parameter, β, provides a method of classifying layers based on the Poisson ratio. While values for α generally fall within the range of $-1 \leq \alpha \leq 1$, values for β typically lie between $0 \leq \beta \leq 0.25$. Since most analyses do not require knowledge of the mismatch in properties other than the modulus (e.g., Poisson

ratio), the first parameter, α, is often more relevant, while the second parameter is either neglected or assumed constant in most bilayer configurations. However, some analyses such as crack propagation analyses may apply the β term.

The effectiveness of the Dundurs' parameters is best illustrated in a comparison of two configurations: One bilayer configuration consists of two metals: steel, the substrate, and copper, the film. The other configuration consists of a polymer and a metal: PDMS, the substrate, and gold, the film. In the first configuration, while steel has a modulus of $\sim$200GPa and a Poisson ratio of $\sim$0.3, copper has a modulus of $\sim$114GPa and a Poisson ration of $\sim$0.3. For the second configuration, while PDMS has a modulus of $\sim$3MPa and a Poisson ratio of $\sim$0.5, gold has a modulus of $\sim$79GPa and a Poisson ratio of $\sim$0.4. Substituting these values into the equation for the Dundurs' parameters results in values that reflect the role of a modulus mismatch in bilayers; the steel-copper bilayer has a relatively low modulus mismatch reflected in the α value of 0.27 compared to that of the PDMS-gold, which is $\alpha = 0.99$. It is also important to note that switching the materials in each layer results in a change in the sign of the Dundurs' parameters, but it does not change the absolute value.

In summary, the parameters act as a measure for explaining the degree of mismatch. The closer the α value is to 1 or -1, the higher the modulus mismatch. This thesis focuses on bilayers with an α value close to 1; the high mismatch of this class of bilayers creates several complications that will be discussed in the following sections. From experiments that will entail the use of a limited number of materials and bilayer configurations, this study will introduce principles that could theoretically be applied to a wider array of bilayer configurations with similar values of Dundurs' parameters.

1.4 Nanoporous Metals: Synthesis and Applications

Nanoporous metals consist of a defined 3D network of pores and struts, the size of which does not exceed a few hundred nanometers. As shown in Figure 1.6, there is much

room for versatility in the design of these structures, which allows them to be tuned to specific applications [38, 39]. The porosity in these materials can introduce additional functionalities [40]. This property is particularly relevant with bilayers of nanoporous metals and elastomers as it entails a reduced property mismatch between the two layers.

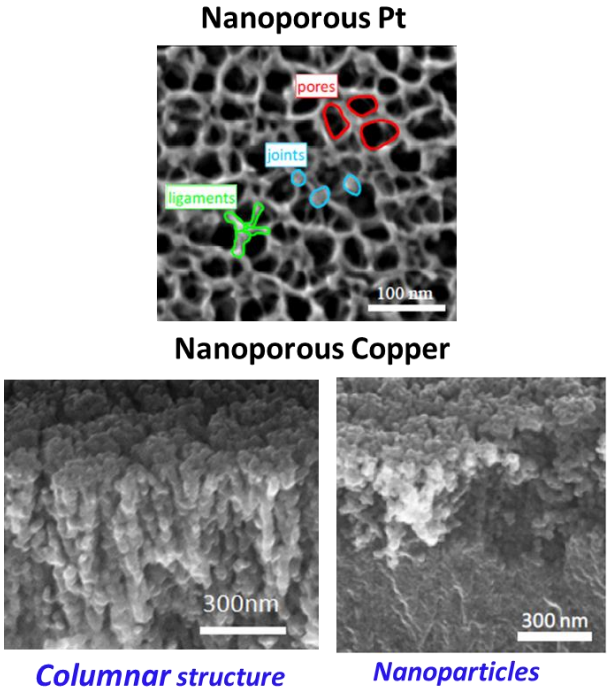

Figure 1.6: Nanoporous Metal Structures [38, 39]

The benefits of nanoporous metals are not limited to the alterations in mechanical properties. In fact, some of the most versatile and widely adopted applications of nanoporous metals take advantage of the increased exposed surface area that results from the pores and struts as well as the unique atomic behavior in these pores and struts [41-43]. This is particularly beneficial in processes that require surface reactions. Some of these applications, demonstrated by other researchers, are shown in Figures 1.7 – 1.9. In Figure 1.7, Kraehnert et al. show the use of nanoporous metals as catalysts for a chemical reaction [44]. Biener et al. and Detsi et al. show in Figures 1.8 and 1.9 respectively, applications of nanoporous metals as actuators under unique stimuli [45, 46]. In Figure 1.7, the actuation

process allows for use as a sensor of ozone and carbon monoxide while in Figure 1.8, with the incorporation of an electroactive polymer used to coat the ligaments of nanoporous gold, mechanical work is possible with the application of electrical stimuli.

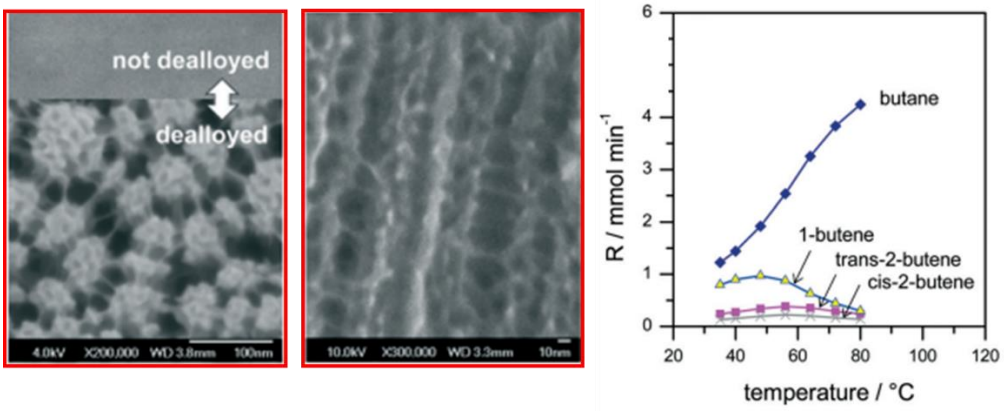

Figure 1.7: Applications of Nanoporous Metals as Catalysts [44]

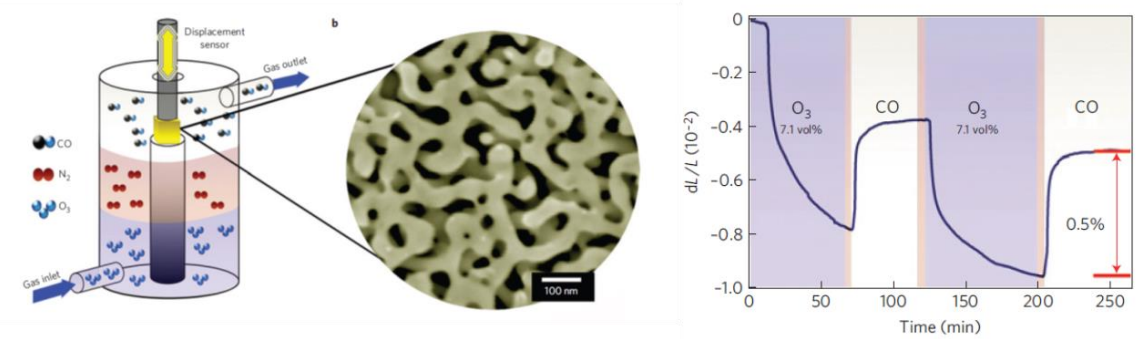

Figure 1.8: Application of Nanoporous Metals in Sensors [45]

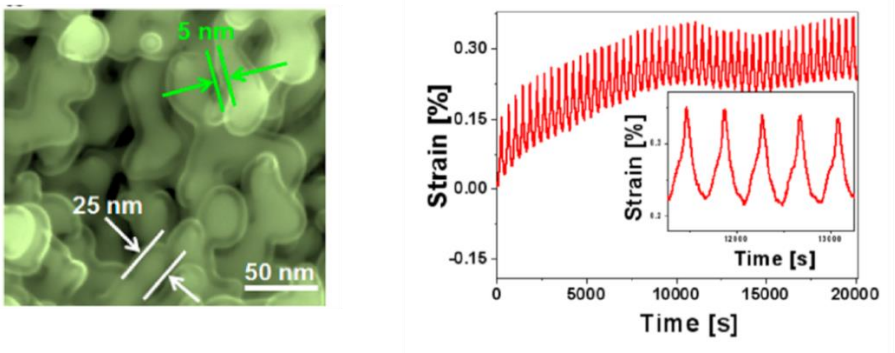

Figure 1.9: Nanoporous Metals Applied in Metallic Muscles [46]

1.5 Motivation for the Performed Work: Challenges with Fabrication

The main motivation for this work is the need to understand some challenges that result from attempting to create bilayers of nanoporous metals and elastomers. The previous sections have presented some of the unique benefits of bilayers and nanoporous metals that allow them to serve a wide range of applications that merge the unique properties of high mismatch bilayers and nanoporous metals. It is however necessary to develop a good grasp of the fabrication process, especially as it relates to failure development. This thesis aims to examine these challenges in fabrication with the goal of providing better control over the process.

1.5.1 Fabrication of Nanoporous Metals

To serve as a background for explaining the source of these challenges, this section outlines the basic approach for fabricating nanoporous metals. Figures 1.8 and 1.9 help illustrate the basic fabrication process for the nanoporous metals. In general, nanoporous metals are created in an electrochemical process called dealloying. The dealloying process makes use of an electrochemical setup. An electrochemical cell is a system of two conducting electrodes undergoing half reactions (oxidation at the anode and reduction at the cathode). The site of the respective reaction depends on the nature of the electrode and can be determined by the electrode potential. The direction of electron flow in this cell is determined by the relative values of the electrode potentials on the galvanic series [47]. When a potential is applied to this system, current is generated by the oxidation of the anode to release electrons, which are conducted to the cathode for reduction. Ions in the electrolyte undergo reduction in the cathode. Under ideal circumstances, the oxidation of ions in the anode could eventually lead to dissolution or loss of mass in the anode, while a sufficient supply of metal ions in the electrolyte or from the dissolved anode could lead to deposition or increase in mass on the cathode. The latter process results in the more common electroplating process while the former is the mechanism involved in

electrochemical dealloying. More information on the electrochemical principles can be found in referenced literature [48, 49].

The dealloying process undergoes a similar electrochemical process. The main difference is the nature of the samples used. In the simplest form, the dealloying process can be explained as a regular electrochemical process as described above, whereby an alloy is used in the working electrode. With a significant difference in nobility for the two components of the alloy, under the right dealloying conditions, one of the components of the alloy becomes more susceptible to dissolution. The result is an extraction of one component of the alloy leaving behind a foam of the other component. The typical sample setup is as illustrated in Figure 1.10.

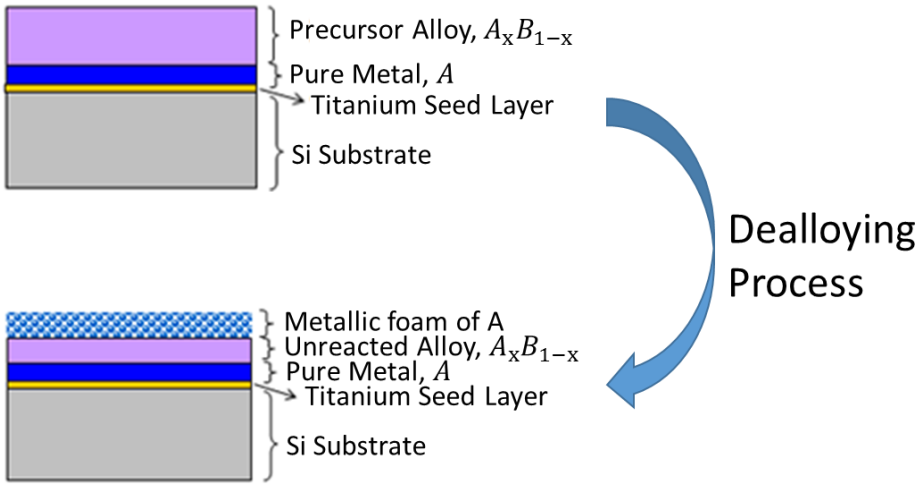

Figure 1.10: Summary of Dealloying Preparation Setup

1.5.2 The Challenge of the New Frontier

Following the explanation in the previous subsection, one could understand that in order to achieve our goal of creating bilayers of a nanoporous metal and an elastomer, we need only substitute an elastomer for the Si substrate in Figure 1.10 and then carry out the same process of dealloying. However, this is not a trivial task: Silicon is a brittle solid that has a low modulus mismatch with the deposited alloy, which in the example is an alloy of silicon. Replacing this silicon substrate with a compliant elastomer would impose a

significant level of property mismatch on the bilayer system, one that could result in instabilities. Such high levels of property mismatch have generally been avoided so little is known of what to expect in such a configuration, hence the need to study the instabilities in high-property-mismatch bilayers. In this thesis, we examine some of these instabilities; particularly, those associated with high stresses, leading to the development of cracks and wrinkles on the bilayers.

1.6 Thesis Organization

The applications presented illustrate a few of the many current and potential applications of polymer bilayers. The purpose of this thesis is to expand on the knowledge of bilayers in this regard.

The thesis is outlined as follows: Chapter 2 begins by presenting the details of the preparation process for these bilayers. This information is necessary because it illuminates the possible contributors to the observed features. Chapter 3 follows with added considerations that support some of the hypotheses we later present, and Chapter 4 discusses the test samples used in detail, as well as their unique behaviors, providing an explanation for such behaviors. Chapter 5 closes with some added considerations that could fuel further study.

CHAPTER 2

SAMPLE PREPARATION PROTOCOL

2.1 Overview

To meet the objectives posed in this thesis, we examine several samples, uniquely designed to address certain questions, and report on their behavior and our conclusions. These samples are bilayers of the polymer, poly (dimethyl siloxane) (PDMS), and a metal alloy. This chapter presents details of the synthesis process including information on the sample compositions and the techniques used. The purpose of the chapter, in addition to presenting the reader with the details of the fabrication process, is to provide background knowledge necessary for the uninformed reader to understand the discussions that follow in subsequent chapters. The information also explains the rationale behind fabrication decisions and conclusions, essentially sharing the train of thought adopted in the experimental process and providing the reader with a starting point for further exploration into the challenge discussed. Observations and conclusions drawn in this study are closely related to factors in the fabrication process, so later portions of the thesis will include multiple references to principles in this chapter.

2.2 PDMS Preparation

2.2.1 Overview

Poly (dimethyl siloxane), commonly referred to as PDMS, is a silicone elastomer used in a host of applications for its many beneficial properties. In the field of microelectronics and micro-/nano- device fabrication, some of its particularly relevant properties are its low cost, optical properties (transparency in the visible spectrum), thermal stability, low modulus with durability, and ease of fabrication [50]. PDMS can also be

molded very easily to create fine features in the micro scale with tolerances within the nanometer range. This quality, coupled with other factors, such as its hydrophobic and physiological inertness, makes it perfect for applications in medical devices and microfluidics. These factors, coupled with the ease of fabrication, make it the most viable option in creating flexible bilayers with sizes in the micro scale that are capable of undergoing large deflections, hence its adoption in the sample designs discussed in this thesis.

2.2.2 Preparation

The raw material for PDMS fabrication is a two-part mix of a base (monomer) and a curing agent (cross linker), both liquid at room temperature. Adding the curing agent to the base facilitates crosslinking of polymer chains to create a dense polymer, solid at room temperature. The ratio of the curing agent to the polymer base is particularly important, and discussions of fabrication routes must include the ratio adopted. Curing could be done at room temperature over a length of days or at elevated temperature to facilitate rapid curing. The PDMS used in this study is the well-known Sylgard® 183 manufactured by Dow Corning. Preparation as outlined by the manufacturer involves two major steps: mixing the base and curing agent in a set ratio and curing at a suitable temperature for a length of time dependent on the curing temperature. The most common curing ratio used for this polymer mix is the 10:1 ratio by weight of base to curing agent; however, researchers have prepared PDMS at other ratios, often to alter the mechanical properties [28, 51]. An added step of shaping in a mold can be included prior to curing since forming is best done while the polymer is in the uncured state.

PDMS preparation in this project seeks to create thin layers of PDMS, several microns thick. Such thicknesses are challenging to obtain with a mold and so in lieu of one, the samples are spin coated on a glass slide to create a film of the desired thickness. Selecting the glass slide as the substrate allowed for easy handling, as it was small enough

to fit in a spin coater and most characterization tools. In addition, with the use of a glass-cutting scribe, samples could easily be shaped to smaller sizes for other applications without the need to separate the PDMS from the substrate. More important however, the glass substrate could withstand the high temperatures that the PDMS may need to be exposed to during the curing step.

In some post fabrication steps, it was necessary to release the PDMS from the substrate for further analysis. In such cases, conventional means of release, such as mechanically with tweezers, could damage the sample in the process. To avoid this shortcoming, a sacrificial layer of poly (acrylic acid) was incorporated between the PDMS and glass substrate layers. This layer was prepared on the glass slide prior to the deposition of PDMS. PAA is manufactured as a viscous liquid, but upon drying, it becomes rigid and readily dissolves in water. This makes it ideal as a sacrificial layer: Created samples with the dried PAA layer between the glass surface and the PDMS need only be immersed in water, causing the PAA to dissolve and the PDMS to float off from the glass slide. As with the PDMS, this PAA layer is created by spin coating liquid PAA and drying on a hot plate prior to PDMS deposition.

Two essential variables considered when preparing the PDMS, the thickness and the modulus, are varied in the fabrication steps. The thickness is determined by the spin speed during the spin coating step while the modulus is dependent on curing temperature. To calibrate the relationship between the spin speed and the resulting thickness, PDMS was first prepared at various spin speeds. Sections were then cut into the PDMS creating steps in the surface profile, over which a profilometer was passed over. The depth of these steps, once read, gave the thickness of the PDMS sample. The homogeneity of the thickness across the entire glass substrate was assessed by measuring the thickness at several positions on the glass slide. The thickness was averaged and plotted versus the spin speed to give a curve that relates the spin speed to PDMS thickness. Figure 2.1 shows the array of steps made on the glass slides for measurements. Actual values are presented in Table

2.1 while Figure 2.2 shows a plot of these averages. The error bars represent the standard deviation of the measurements and give an idea of the homogeneity of samples prepared at each thickness. The standard deviation of the measurements, which is related to the level of roughness/unevenness in the PDMS, is presented in Figure 3 against the measured thickness. The unused region in Figure 2.1 represented a portion of the sample that may have been damaged due to handling. In a few cases, read values were erratic, possibly due to poor separation of the PDMS from the substrate or extensive damage. These outlying values were omitted from measurements to give the most accurate depiction of the thickness. The omitted values are shown as blanks in table 1.

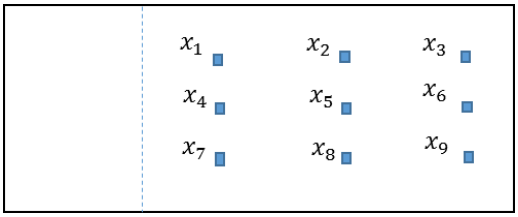

Figure 2.1: Average Step Positioning for Thickness Measurements

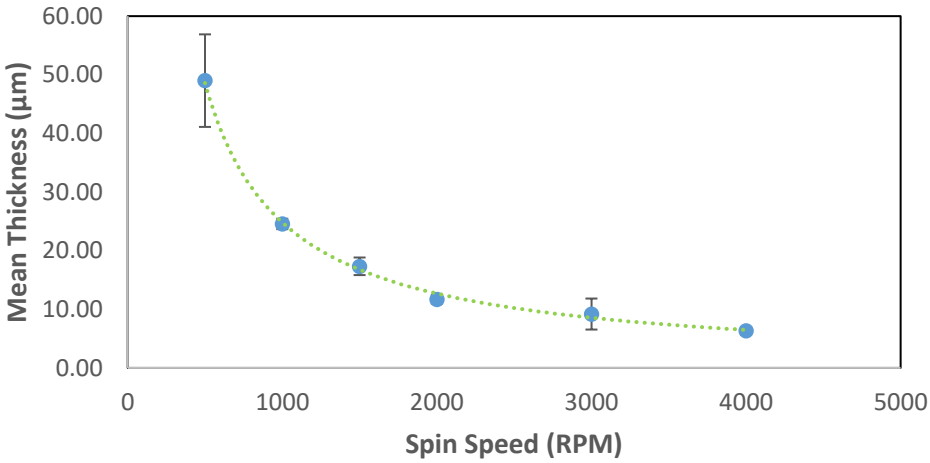

Figure 2.2: Average Measured Thickness vs. Spin Speed

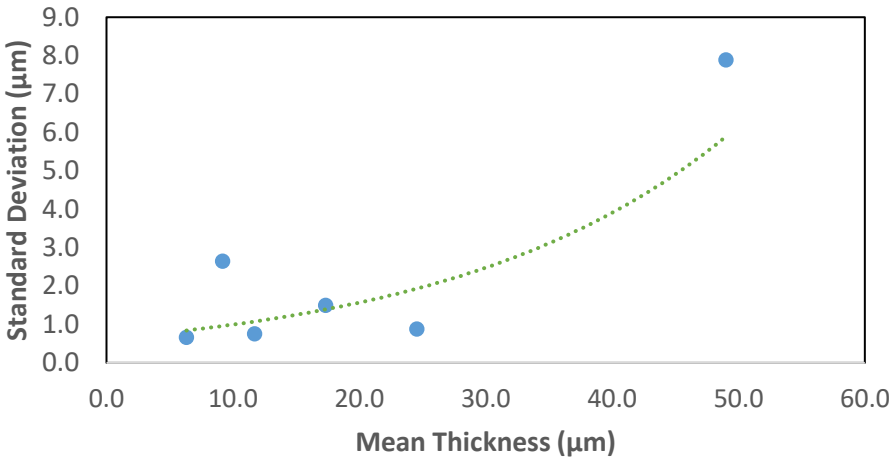

Figure 2.3: Standard Deviation of Thickness Measurements with Mean Thickness

The curing temperature of the PDMS also plays a role in the properties of the final sample, affecting the modulus of the PDMS. This relationship is however well understood and reported by manufactures and other researchers who have conducted extensive research into the matter. This data was used in characterizing samples from the current study. Three curing temperatures were used: 70, 110 and $150°C$ for samples spin coated at each speed and therefore thickness.

2.3 Metal Film Deposition

Another step adopted in the sample fabrication process involves the deposition of a thin metal film on the PDMS surface. The film, preferably several nanometers thick, would need to have excellent adhesion and conform to the smooth PDMS surface. The property differences between this film and the PDMS will be necessary in facilitating the desired actuation behavior. Magnetron sputtering, a variation of the familiar sputtering technique, is used in creating this film. Although several deposition techniques exist, these all have their respective limitations that make them unsuitable. The most common techniques, most likely to be adopted in creating the types of samples discussed in this

thesis, are the evaporation and sputtering techniques. Of these two techniques, the sputtering technique is selected due to several features that make it better suitable and ideal for this application. These features and other advantages are discussed in the following subsection.

2.3.1 Magnetron Sputtering

Sputter deposition is a form of physical vapor deposition whereby a plasma contained in a sputtering chamber is used to liberate atoms from the surface of a target to be deposited on a substrate [52, 53]. The plasma is an ionic gas created in the sputtering chamber. Also in the chamber are an anode and cathode separated by a void where the plasma will be filled. The pressure in this chamber is lowered and a gas, typically argon due to its inertness, is introduced. When a potential difference is created between the anode and the cathode, electrons are forced to migrate away from the cathode creating a thin potential drop region that causes ions in the gas to accelerate towards the cathode. The impact of these ions on the cathode causes more electrons to be emitted from the surface, which in turn causes ionization of more atoms, growing the plasma. With a high enough energy, the ions in the plasma bombard and liberate atoms from the cathode, which is also fitted with the target material to be deposited. Upon growth of the plasma, ion bombardment of the cathode leads to the liberation of high velocity atoms that travel across the chamber to the substrate, where they settle leading to the development of a film of atoms. More elaborate details on this process can be found in referenced literature [52-56].

As a process that works by ion bombardment in a moderate temperature environment, the sputtering technique has several advantages over other film deposition techniques that are available. Perhaps the most relevant of these to the bilayers discussed are the versatility of the technique, which allows for the deposition of a wide range of metals and alloys, and its compatibility with temperature sensitive materials. The versatility is necessary to deposit alloys without the need for an annealing step (which would be

necessary to create a homogenous film by depositing pure elements separately) while the low temperature requirement is necessary when working with soft materials that have low melting points. Magnetron sputtering works on the same principle as the conventional sputtering technique but with an improvement that incorporates rotating magnets to keep the electrons moving in a loop above the cathode. This added feature increases the ionization occurrences and thus improves the plasma, yield and overall efficiency of the process [54]. The added functionality of the magnetron sputtering technique coupled with the already established benefits of the sputtering technique makes this an appropriate method for deposition on the temperature sensitive polymer considered in this study.

2.4 Ultraviolet (UV) Ozone Treatment

UV-Ozone treatment is a process adopted in several microelectronic procedures, primarily for cleaning substrates and surfaces by removing organic materials that may serve as contaminants or that may hinder subsequent processing steps. The method could however present inherent problems of its own, generally unique to the specific application. An understanding of the underlying chemistry of the process can help to inform a designer to avoid undesirable outcomes and explain any curious observations.

Ultraviolet radiation refers to the electromagnetic waves with wavelengths within the ultraviolet range of the electromagnetic spectrum, just below the wavelength range of visible light. This lower wavelength implies a higher frequency and thus a higher energy with greater potential to dissociate molecules. Oxygen (O_2) is an example of one such molecule. UV light with a wavelength of 184.9nm is absorbed by O_2 to create the more reactive Ozone (O_3). Organic molecules such as oils or resist materials could also absorb UV radiation and undergo photosensitized oxidation processes. The UV cleaning process uses this approach, working on an atomic level to remove certain contaminants. The process requires both the presence of UV radiation often generated using a mercury (Hg) lamp and an ample supply of oxygen, which serves as fuel for ozone generation [57]. With

an appropriate wavelength UV source to dissociate atoms and an ozone source to react with dissociated atoms and thus aid removal, the UV treatment technique serves as an efficient method of cleaning surfaces of resists or general impurities; however, it also has potential to modify the substrate being treated. More details on this modification is discussed in Chapter 3.

All of the steps discussed are applied in the development process of the bilayers used in this study. With each step comes its own limitations and contributors to the unique observations made herein. A detailed description of the bilayer development process as they apply to these processes and an in depth look into the effect of the effects on the resulting bilayer is presented in chapter 4. This will help aid the main discussion of this thesis.

CHAPTER 3

PROCESSING PARAMETERS

This chapter presents a brief overview and background of the crucial factors that could affect the resulting nature of bilayers. This information will serve as a backdrop and reference in the discussion of the causes of certain instabilities.

3.1 Surface Modification by UV-Ozone Treatment

An essential factor to consider is the surface modification that results from UV-Ozone treatment. UV treatment of polymers held much promise as a technique for cleaning polymer surfaces, but with the ongoing discovery of its unusual effects on polymers, the technique has also become an avenue for surface layer modification of polymers. With this modification comes several property changes such as altered hydrophobicity and improved adhesion to deposited materials. Although the removal of impurities could explain some of these factors, the primary cause of these modifications lies in the altered chemistry of a thin surface layer of the polymers. During UV treatment in the presence of Ozone, UV light provides energy needed to facilitate the bonding of oxygen and other radicals to polymer chains. The result is a modified polymer chain structure that takes the chemical form of a silicon oxide. This modified composition could result in a denser or more brittle surface layer, among other possible changes. Changes generally extend below the surface by a few nanometers or as deep as several microns into the PDMS, creating a thin film of modified polymer, the thickness of which is known to be dependent on the length of exposure and degree of crosslinking in the PDMS. This thickness, although, small and seemingly insignificant, is sufficient to create changes in surface behaviors that could affect the behavior of samples. More details on these effects as well as the detailed chemistry, mechanism and changes in specific polymers can be found in numerous reports that have

delved into the matter [58, 59], but for the sake of this thesis, focus will be kept on the effects on the polymer Poly (dimethyl siloxane) (PDMS).

For the bilayers in this study, the effect of concern is the surface modification that could lead to an altered modulus and possibly a change in the strain state. Because the level of modification due to the treatment process is not clear, we rely on calculated assumptions based on observations in this and other studies on the matter. The effect on hydrophobicity, and hence on the level of adhesion incurred, is explored. Specifically, the importance of this step in promoting adhesion of a deposited film is evaluated using a control sample that was developed without the UV-Ozone treatment step.

3.2 Temperature Effects of Sputter Deposition

Another factor that needs to be considered when attempting to understand the stresses in bilayers is the effect of thermal loads during preparation. This factor is especially important when the materials involved have a significant difference in thermal expansion coefficients, as is the case with the samples considered in this thesis. Polymers, with their high thermal expansion coefficients even at low temperature, are susceptible to significant deformation during many processing steps. This deformation could be a source of intrinsic stressed, as discussed in Section 1.3.1. Therefore, if there is a remote possibility that thermal factors may be present, the possibility needs to be explored. However, a review of sputtering effects showed that thermal effects are not a significant issue during the deposition stage [60]: Sputtering, unlike some other deposition techniques, does not rely on high temperatures to facilitate deposition. Instead, substrate temperature rise is a result of the kinetic energy of impeding atoms. Few studies have attempted to quantify this effect but results show negligible temperature rise in the substrate [60]. For this reason, in the studies discussed in this thesis, temperature effects due to the sputtering process are considered negligible and are not considered as a relevant factor to understand results. The curious researcher could however probe into these effects.

3.3 Residual stresses due to sputter deposition

Although thermal stresses are not considered as a limiting factor in the sputter deposition process, we did recognize that stresses could develop due to other mechanisms. As with other deposition techniques, unique elements of the sputter deposition process could often serve as limitations to the technique. Explaining these limitations requires an understanding of the development process. Incident atoms on a sputter deposition substrate are often referred to as adatoms. These adatoms, upon reaching the surface, could settle and adhere to the substrate, or with sufficient energy, maintain some mobility on the surface. Eventually however, the adatoms settle into an equilibrium state and the growth of the films begins.

Film growth may either be polycrystalline or epitaxial. Epitaxial growth occurs when there is a close match in the lattice parameters. For an amorphous substrate like PDMS, it is impossible to obtain a lattice match with a deposited metal. Growth in this case thus follows a polycrystalline nature, beginning with the nucleation of adatoms to form islands that eventually grow large enough to form a continuous film, as illustrated in Figure 3.1. The details of this development process is additionally dependent on the energy involved as affected by surface and interfacial properties; a developing system seeks the lowest energy configuration for development. Island growth for instance is affected by the relationship between the interfacial energy between the adatom and the substrate and the energy between two similar adatoms; if the interfacial energy exceeds the material energy, growth is more favorable on already existing islands, and vice versa.

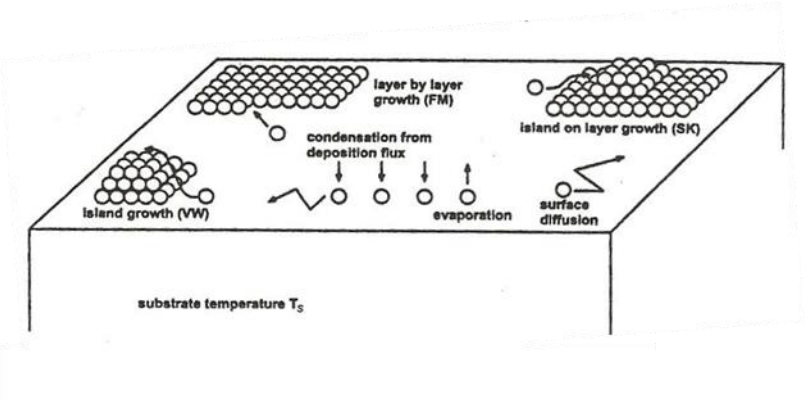

Figure 3.1: Typical Film Growth Process [61]

These basic principles have served as an explanation for the intrinsic stresses that develop during film growth. Unlike extrinsic stresses that arise because of external factors such as temperature change, intrinsic stresses are more inherent to the development technique and material properties. Typically stress developments follow the general pattern illustrated in Figure 3.2, extracted from reference [61], beginning with a compressive stress that steadily grows into tensile stresses before a final drop. A general hypothesis that explains this behavior attributes the initial compressive stresses to the initial growth of the islands. Upon initially impinging on the surface, adatoms are fixed to the surface and growth of islands is restricted to the initial fixed site. With time however, the hypothesis explains that further growth leads to tensile stresses that develop as a result of energy conversation that converts gaps between islands into grain boundaries. More time allows for a denser packed film that results in compressive stresses. The details of the levels of stresses following this pattern would however depend on the nature of the film being deposited.

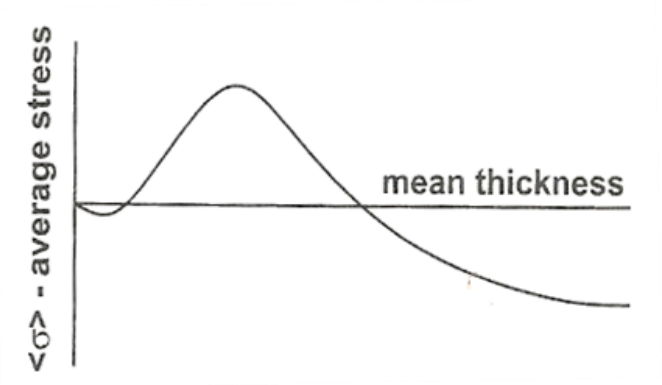

Figure 3.2: Stress Development Pattern for Polycrystalline Films

3.3.1 Surface Energies and Mobility of Adatoms

The major factor to consider in the sputtering deposition is the effect of the mobility and energy of ions and electrons. The energy of the ions impinging on the target, determined by the potential in the sputtering system, determines the sputter yield. This in turn affects the energy of the liberated atoms and affects the nature of the surface created; high-energy atoms have greater mobility upon reaching the surface of the atom. This in turn determines the development of the film. Likewise, high-energy atoms could lead to damage of the substrate, which may have secondary effects on the nature of the bilayer once developed. The energy of the ions is controlled by the potential difference in the sputtering setup. Typically, the level of stresses that result from the atom mobility is understood by the sputtering technician and is for the most part, independent of the sputtering chamber. This allows the technician to control the intrinsic stresses to be expected on the bilayer. The adatom energy does however play a less understood role unique to polymers and similar substrates. Studies have found that high energy atoms from the sputtering process are likely have an effect similar to the UV process [62]. Atoms can be implanted into the PDMS, modifying the surface layer in ways that are not fully understood. This could result in effects unique to the materials involved and difficult to quantify.

CHAPTER 4

CRACKS AND WRINKLES IN BILAYERS

4.1 Introduction

Wrinkling and cracking have attracted increased interest because of their potential as nanostructured pattern fabrication routes that would, for instance, render a surface hydrophobic [63-65], allow for the fabrication of microfluidic circuits [66] or aid in the design of flexible electronics [2, 67, 68]. Regardless of the motive for creating such bilayers, a reliable fabrication route is necessary, hence the importance of information on bilayer conditions developed under certain fabrication conditions. Although several guidelines in design have been documented [18, 61] these either describe a more general situation or focus on another configuration from the one we might be discussing. As a result, a great deal has yet to be explained. The goal of this chapter, therefore, is to clarify much of the confusion surrounding the instabilities created on the bilayers that we discuss, and in the process, to supply the bilayer designer with information needed to control experimental outcomes. To accomplish this goal, this study introduces two crucial factors: First, we need to establish an optimum processing window for these structures so that the maximum possible stresses can be locked at the interface while preventing excessive damage, and second, we need to present guidelines on how to intentionally create cracks and/or wrinkles in a controlled way.

To properly examine bilayer instabilities (cracking and wrinkling), we adopted an experimental approach whereby we created several samples under carefully selected conditions and evaluated the condition of the samples after fabrication. This approach was necessary because of the nature of the task: Since the factors that cause these instabilities are not apparent, any model created would likely be flawed as all factors and mechanisms cannot possibly be accounted for. This chapter presents the details of our experimental

process, including the rationale, experimental approach, and findings. The study illuminates the contribution of specific mechanisms; by keeping selected conditions constant, we isolated the potential cause of certain behaviors, narrowing down the relevant mechanisms that could subsequently be incorporated into a model for verification purposes. One such model is introduced in later parts of this chapter, to verify assumptions we made and evaluate these assumptions against experimental results.

The analysis that follows focuses on instabilities created due to interfacial mismatch strains that form when silicide or metal-alloy films were deposited on polymer substrates. In general, thin coatings deposited on a substrate to form a bilayer, can span a wide range of coating thicknesses, from the 10^{-1}m range for paved roads, to the 10^{-9}m range for integrated circuits. For all of these cases, mismatch strains locked at the interface can be formed at any point in the deposition process and residual stress build up can be relieved via various energy release mechanisms, including delamination [69], wrinkling [1-3] or crack formation [6]. Phase diagrams for various instability patterns [35] formed at the surface under compressive mismatch strain account for wrinkles, folds, creases, and ridges depending on the elastic moduli ratios of the coating and substrate[70-72]. Cracks can also form when the interfacial strength is weak, resulting in coating delamination and crack formation [6]. However, under tensile mismatch strains, intricate crack networks, involving multiple parallel and intersecting cracks can form [6, 73]. To understand these instabilities, we focus on characterizing the surface patterns formed on bilayers, specifically those involving a metal alloy or metal-silicon alloy coating sputter deposited on thin elastomeric substrates such as polydimethylsiloxane (PDMS). These fall under the general category of bilayers with extreme modulus mismatch (Dundurs' parameter values of $\alpha \cong 1$ and $\beta \cong 0$) and strong interfacial adhesion, a bilayer configuration that is currently not completely understood. Thus, the key condition of interest is strong interfacial adhesion at the bilayer interface coupled with substantial property differences between the coating and the substrate.

Aside from the effects of the wide variation in Dundurs' parameters, the development of strong adhesion is explored through ozone treatment and the sputter process. Finally, the effect of the coating fracture toughness and the substrate characteristics, including the thickness and surface chemistry, are examined. The chapter is thus organized as follows: We first present the experimental protocol followed by a discussion of the experimental results, beginning with a brief theoretical background to aid the discussion of the results. In the discussion, we present information based on existing studies and along with a new hypotheses associated with the bilayer configuration, backing these up with the results from the experimental studies where necessary.

4.2 Experimental Protocol: Summary and Details of Samples Prepared for this Study

In our study of the cracking and wrinkling effects on bilayers, the test samples consisted of two layers. The PDMS layer, prepared in a 10:1 ratio by weight of monomer to cross linker, was created by spin casting Sylgard® 184 on a rigid glass slide using a Laurell spin coater. A layer of poly (acrylic acid) (PAA) film was first spin casted between the PDMS and the glass slide, prior to PDMS preparation. Spin casting was done at 1,500 revolutions per minute (RPM) for one minute for a 25 wt% PAA aqueous solution, followed by drying at 100°C for 30 minutes. The PAA layer was added solely to aid in the release of samples, when necessary, without introducing unwanted stresses. A range of spin casting speeds were used in the fabrication of several samples with various PDMS film thicknesses. The correlation between spin speed and the thickness of the PDMS samples was obtained following the calibration experiment described in Chapter 2. Based on this information, spin speeds of 0.5K to 4K RPM resulted in PDMS thicknesses between 30 and ~6 μm, respectively. The homogeneity of the thickness across the entire glass substrate, which was assessed by measurements of the thickness at several positions on the glass slide, showed thickness variations of ~8μm for speeds of 0.5K to 1K RPM and 0.6μm

for a speed of 4K RPM. Three curing temperatures, 70°C, 110°C, and 150°C, were used for samples spin coated at the same speed and thickness. Since studies have shown that the PDMS modulus is temperature dependent, each of these curing temperatures resulted in a unique modulus [74].

The next step, following PDMS preparation, is the metal-alloy deposition step. Prior to this step, the majority of the samples underwent the UV-ozone treatment process discussed in Chapter 2. These were exposed to ultra-violet (UV) ozone irradiation using a Jelight Company, Inc. Model 42A UVO Cleaner. Irradiated samples were exposed at an approximate distance of 2cm from the UV source. Some samples were not irradiated in order to examine the impact of the UV-Ozone treatment step on the eventual surface morphology. The metal alloy coatings were deposited using magnetron sputtering under 100V DC bias. A 5nm Ti seed layer followed by an alloy of either gold-silicon (Au-Si) or gold-silver (Au-Ag), depending on the sample, were deposited on the PDMS and prepared to a thickness of 70nm.

The sample deposition conditions are summarized in Table 4.1, which lists PDMS thickness, the curing parameters, and UV treatment that identify the samples. The alloys consisted of $Au_{0.2}Si_{0.8}$ and $Au_{0.3}Ag_{0.7}$ by atom percent (at. %) as validated with X-ray photoelectron spectroscopy (XPS). Residual stresses, introduced as a result of the sputter deposition process, were accounted for based on preliminary experiments: Prior curvature change measurements with a laser-scanning apparatus found that coatings of this type, sputtered under similar conditions on rigid silicon substrates, exhibited 100-200 MPa residual compressive stress in the thin films after deposition[75, 76]. Given that the only difference between these two deposition processes (i.e., the curvature measurement and our sample depositions) was the substrate, we assume that the stresses introduced in our samples have the same order of magnitude.

Table 4.1: Description of fabrication parameters of samples used in this study

Sample ID	PDMS Thickness (μm)	PDMS cure ($°C$)	UV Treatment	Metal alloy type
6/70 PDMS/Au_{20}-Si_{80}	6 ± 1	70	N	Au-Si (20%-80%)
6/150 PDMS/Au_{20}-Si_{80}	9 ± 3	150	N	Au-Si (20%-80%)
25/110/UV PDMS/Au_{35}-Ag_{65}	25 ± 1	110	Y	Au-Ag (35% - 65%)
25/110/UV PDMS/Au_{20}-Si_{80}	25 ± 1	110	Y	Au-Si (20% - 80%)
6/110/UV PDMS/Au_{20}-Si_{80}	6 ± 1	110	Y	Au-Si (20% - 80%)
50/110/UV PDMS/Au_{20}-Si_{80}	49 ± 8	110	Y	Au-Si (20% - 80%)

The surface characteristics of the films after deposition (e.g., cracks or wrinkles) were examined with optical scanning electron microscopy (SEM) and confocal microscopy. Post processing was done using ImageJ, an image-processing program [77]. The optical images were taken with a microscope camera by Edmund Optics with an EO 5987 lens. As for the cracks, only those that extended beyond intersections were used in the measurements, and any branching events were ignored. SEM images were taken by a Zeiss Ultra 60 FE SEM. At least eight measurements were obtained for each sample and the average value was reported. Confocal microscopy images for some samples were obtained using an Olympus LEXT 3D material confocal microscope. These images served to create a better understanding of the nature of the cracks and wrinkles with respect to the depth. A focused-ion-beam section on one of the samples was used to confirm the through-thickness observations of the confocal microscope. The result and consequences of these sample preparation steps are reflected in the samples. The features of the samples are analyzed, which leads to a more thorough understanding of the effects of the development.

4.2.1 Calculating Strains from Confocal Profiles

Although residual strain conditions of the samples were controlled, some of the resulting samples did not reflect these conditions, which will be discussed in more detail in the following sections. To understand the degree of this deviation and to inform our analysis, we estimated the apparent strain conditions directly based on the results. In order to obtain this estimate, we adopted a profile analysis approach in which we analyzed confocal maps to obtain the degree of deformation associated with the wrinkled surfaces. This approach assumes that because of constraints, expansion deformations of the surface layer results in surface-layer bending, which create wrinkles, as illustrated schematically in Figure 4.1: We assume that the primary energy release mechanism is the formation of wrinkles; therefore, the change in surface features is primarily due to introduced stress. Following this logic, the strain can be estimated by the fundamental strain relationship: $\varepsilon = (l - l_0)/l_0$, where l and l_0 are the final and initial lengths respectively. However, since the confocal maps involve areas, and not 2D lines, as illustrated in Figure 4.1, we used a modified equation for the strain: $\varepsilon = (A - A_0)/(1 - \nu)A_0$. A_0 and A are the initial and deformed areas respectively, as determined from the confocal image analysis, and ν is the Poisson ratio, which is incorporated into the expression to account for differences in strain behavior along the dimensions of the area.

The confocal images were also used in the estimation of the average wavelength of the samples, which was accomplished using an FFT algorithm that analyzed the raw data, smoothened to eliminate noise, as illustrated in Figure 4.2. The result was an FFT, similar to that shown in Figure 4.3, with several peaks that accounted for the hierarchy of the wrinkles. We selected the first two peaks, which reflected the wavelengths. These results were compared to those of the predicted values from literature.

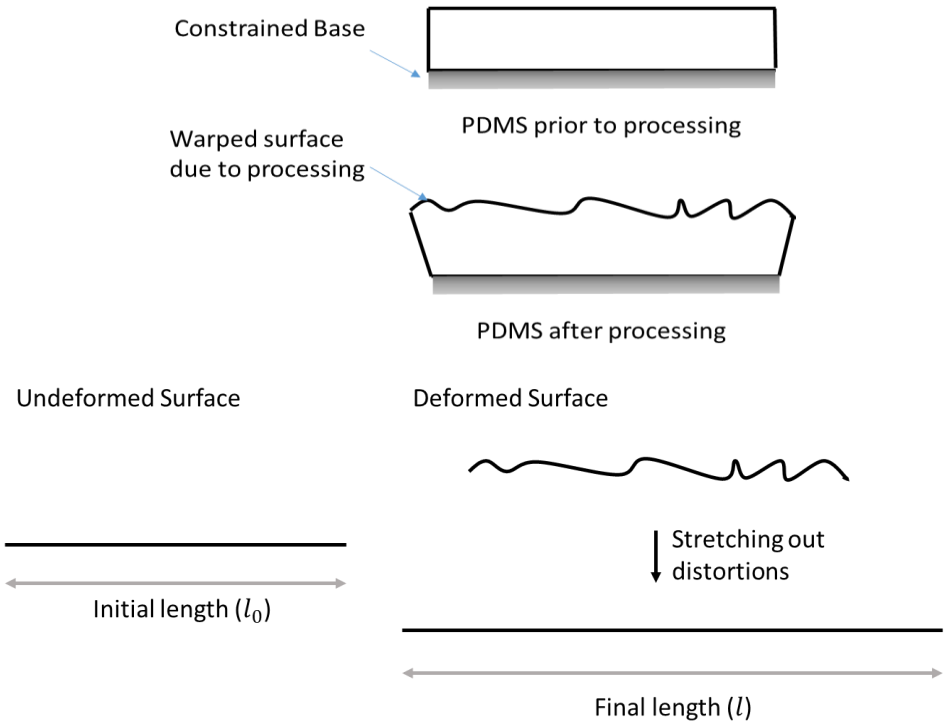

Figure 4.1: Schematic of Principle applied to calculate Strains from Wrinkle Profiles

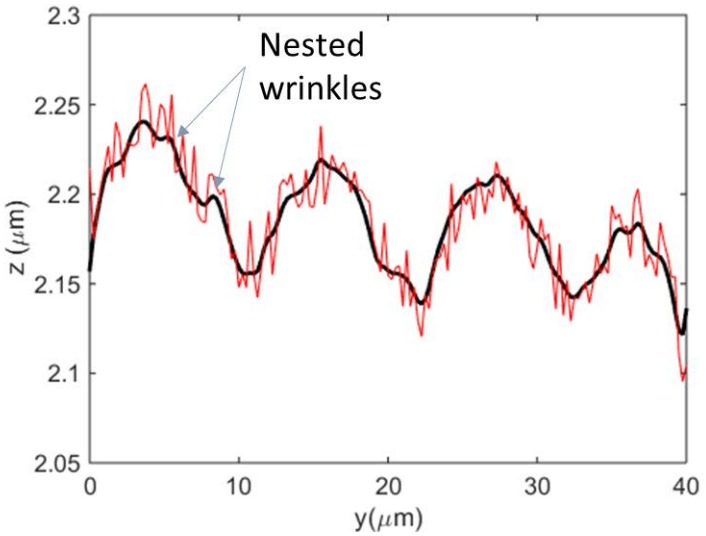

Figure 4.2: Band Pass Filtering of Confocal Data: Filtered vs. Unfiltered Profile

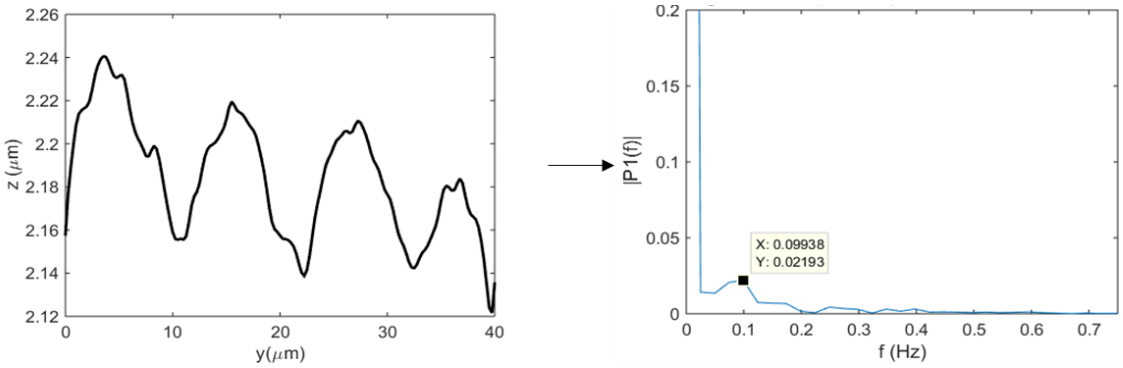

Figure 4.3: Obtaining Wavelengths from FFT of Profiles

4.3 Description and Discussion of Observed Surface Patterns

The samples presented in Table 4.1 were selected to examine the effect of (a) curing temperature, (b) elastomer thickness, and (c) UV treatment on the resulting out-of-plane instability patterns. All samples with Au-Si coating exhibited an array of cracks of varying densities and depths. The Au-Si samples that did not undergo UV treatment prior to sputter deposition had wrinkles in addition to cracks on their surface. The Au-Ag coating exhibited only wrinkles. The characteristics of these patterns and their relationships to the deposition parameters are discussed in the following subsections.

4.3.1 Wrinkle Wavelength and Its Relationship to Existing Theories

Of the samples listed in Table 1, wrinkles were observed on the Au-Ag sample and the two non-UV-treated Au-Si samples. Planar view images of the wrinkles are shown in Figure 4.4. Also shown in this figure is the nested or hierarchical wrinkled network, an observed behavior whereby multiple sets of wrinkles of various sizes appear to form on the same samples, as observed on the Au-Si sample shown in Figure 4.4c. We estimated the average wavelength of these wrinkles from the confocal images, as explained in Section 4.2.1. We noted that these wavelengths were roughly two orders of magnitude smaller than

the characteristic crack spacing, which is discussed in a subsequent section. This observation is crucial to our discussion of the source of these instabilities.

With the wavelengths from confocal profiles, we compared the behavior of our samples to that of the predictions from studies that claim that the wavelength of wrinkles formed under compressive stresses depend on the elastic moduli of the film and the substrate, and on the thickness of the film. Based on these models from the literature, wrinkles begin to form once the compressive film stresses exceed a critical value that induces buckling, determined by

$$\lambda_0 = 2\pi h_{\mathrm{f}} \left(\frac{\bar{E}_{\mathrm{f}}}{3\bar{E}_{\mathrm{s}}}\right)^{\frac{1}{3}}, \tag{4.1}$$

where λ_0 is the critical wavelength. Subscripts f and s represent the properties for the film and substrate respectively; h_{f} is the film thickness, and $\bar{E}_{\mathrm{f}}$ and $\bar{E}_{\mathrm{s}}$ represent the biaxial moduli, which are based on the general expression for the biaxial modulus given by $\bar{E} = E/(1-\nu^2)$. Wavelength values obtained from confocal analysis as well as theoretical predictions based on Equation 4.1 are shown in Figure 4.5: Values are normalized with respect to the film thickness ($70\mathrm{nm}$ for all samples) and expressed as a function of the biaxial modulus, $\bar{E}_{\mathrm{f}}$. The gray region bounded by solid lines represents the predicted values based on Equation 4.1. Figure 4.5 also shows the results obtained from an FEM analysis.

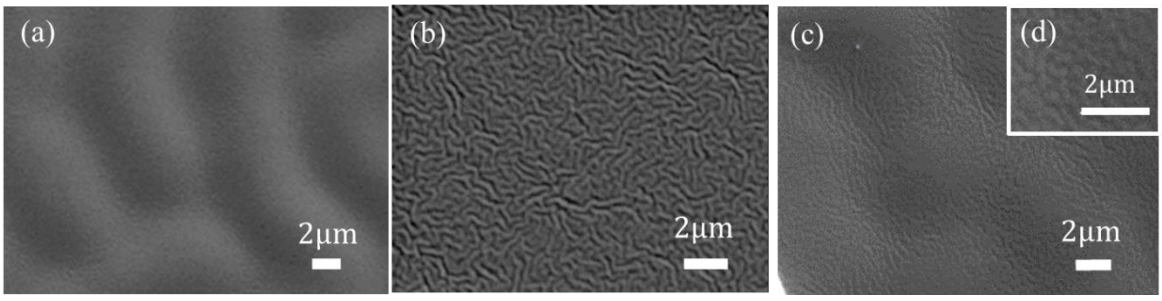

Figure 4.4: SEM Images of the Bilayer Surface after Coating Deposition: (a) 25/110/UVPDMS/Au-Ag, (b) 6/70PDMS/Au20Si80, (c) and (d) show 6/150PDMS/Au20Si80 at two magnifications so that nested wrinkles become clearly visible.

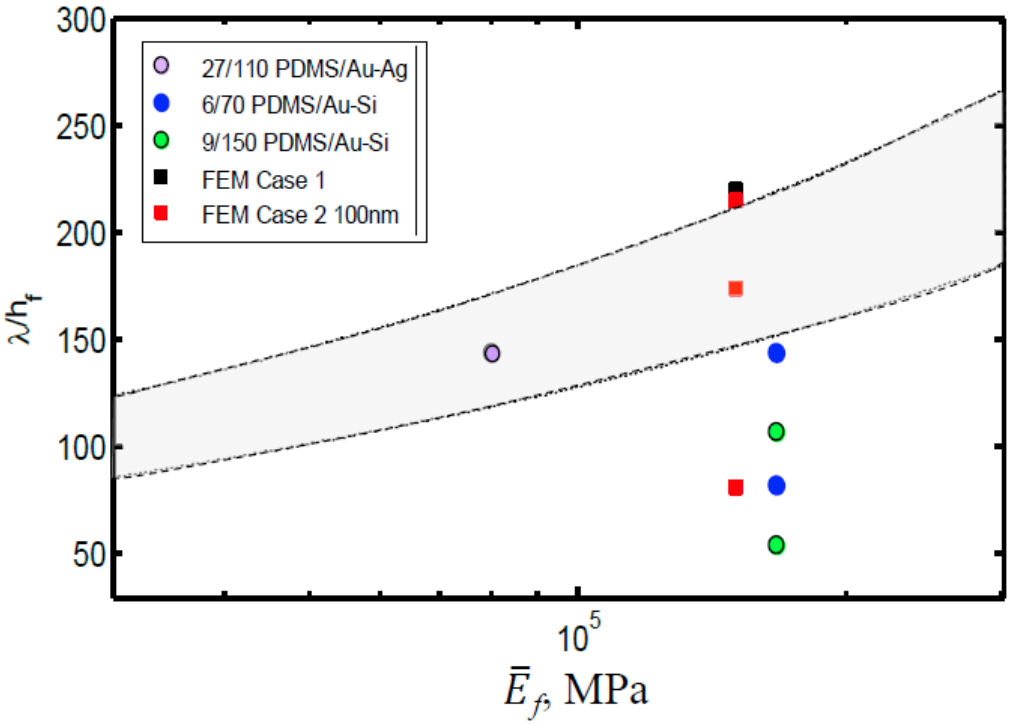

Figure 4.5: Wrinkle Wavelength vs Biaxial Modulus of Film

By comparing the observed results to the theoretical values, we show in Figure 4.5 that the wavelength of the sample with the Au-Ag coating agrees well with the theoretical predictions of Equation 1. Meanwhile, the samples with the Au-Si coating, which have two wavelength values that account for the nested or hierarchical nature of the wrinkles, have wavelengths smaller than predicted. Previous studies have shown that these nested wrinkles can depend on the magnitude of the applied mismatch interfacial strain [78]. However, for the two Au-Si samples showing nested wrinkles of various wavelengths, the only parameter that we varied was the curing temperature, which, as mentioned previously, affects the modulus of the PDMS, in this case varying the value between 1.7 and 2.6 MPa for the two samples. This observation alone could suggest a relationship between the modulus and the interfacial strain or imply a deviation from conventional behavior. We also note that the smaller wrinkle wavelength cannot be accurately captured by accordion-type models, which are presented in literature to describe post-buckling compressive strain

behavior [79] since our models predict a 10% decrease in the wavelength for these material properties, when under additional 10% mismatch strain. In addition, another factor that can affect the wavelength, based on Equation 1, is the film thickness. For the samples used in this study, the film thickness of the Au-Si samples was constant so the reported difference in wavelength shown in Figure 4.5 was most likely a result of the PDMS properties and surface treatment processes.

4.3.2 Crack Network Characteristics

All samples with Au-Si coating formed an intersecting network of parallel cracks after sputter deposition. This phenomenon has also been reported when iron thin films were sputtered on an elastomer [18]. The basic nature of the cracks is shown in Figure 4.6, which includes the confocal microscopy plan view (Figures 4.6(a), (c), and (e)) as well as the height (Figures 4.6(b), (d) and (f)) of the bilayer surface for UV treated samples following Au-Si film deposition. This figure reveals some behaviors that would not have been expected: The plan view confocal microscopy images in Figures 4.6(a), (c), and (e) shows that the density of cracks increases with decreasing PDMS thickness. In addition, as the spacing between the cracks reduces, the out of plane deformation appears to increase, as evidenced by the blurry in-plane confocal micrographs as well as the 3D plots of the out-of-plane height. Close-up images of the cracks on the same samples shown in Figure 4.6 are presented in Figure 4.7. The images in this figure capture the crack depth and opening of the samples.

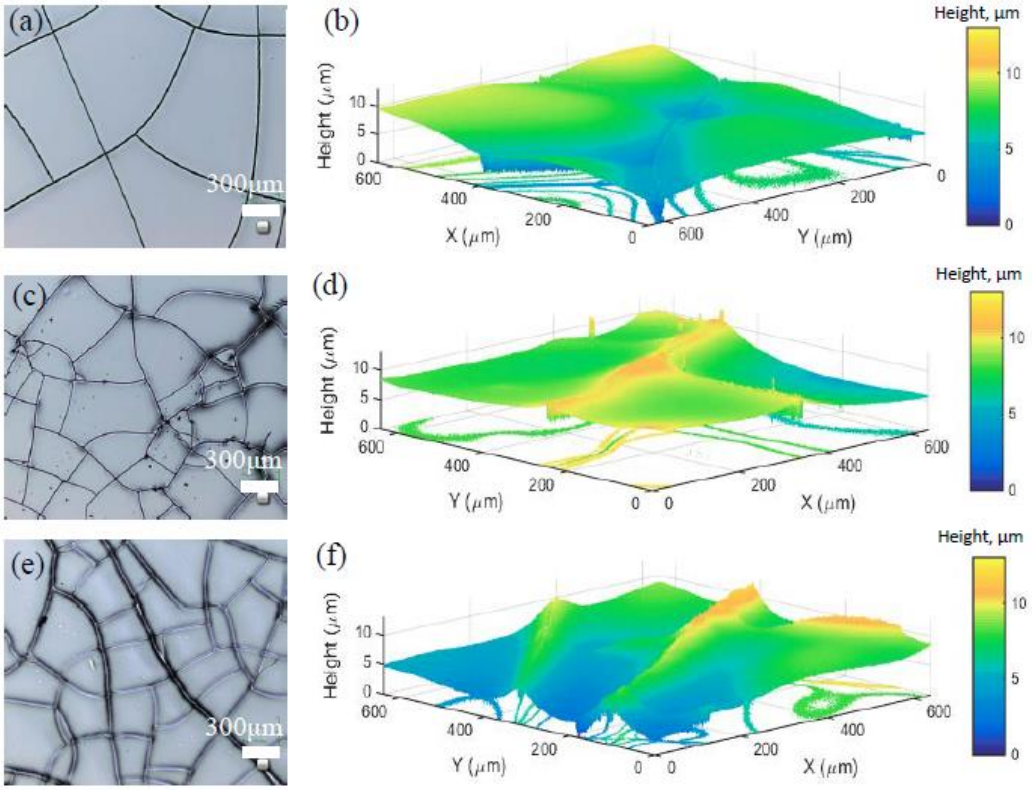

Figure 4.6: Confocal View of Crack Networks on UV Treated Bilayers

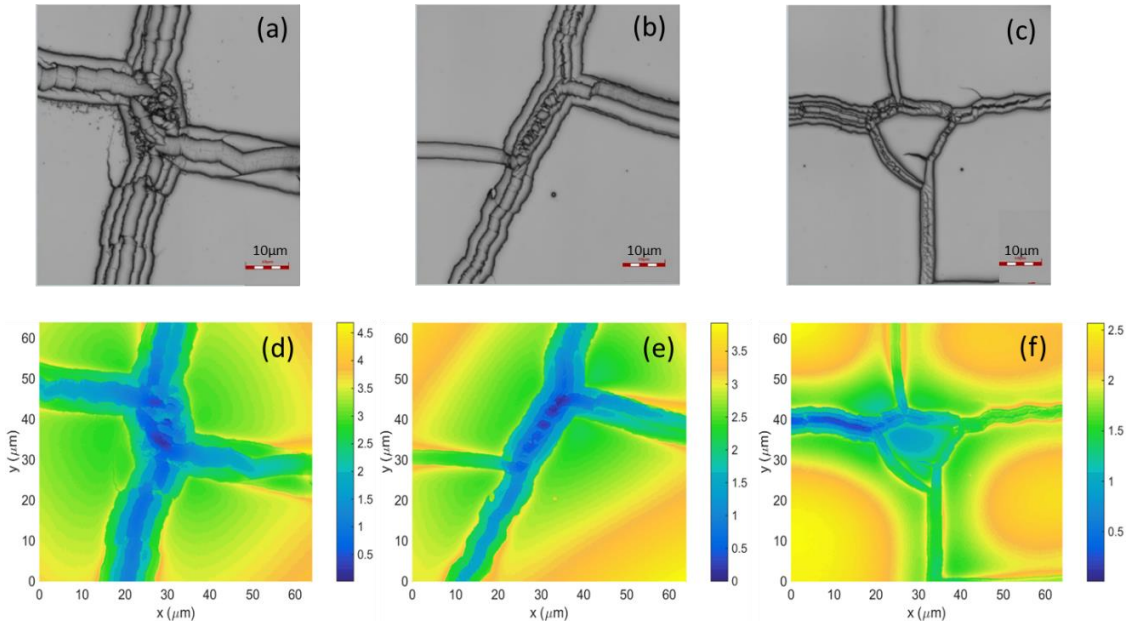

Figure 4.7: Confocal View of Cracks on UV Treated Bilayers

To help understand the variations in crack behavior highlighted from Figure 4.5, we employ the cluster analysis approach, a technique that uses an algorithm to divide a set of points into groups with similar attributes. The technique was used to identify the cracked segments appearing in the images. To perform this analysis, SEM images of the cracked samples were thresholded by brightness exceeding a given threshold to identify the outlines of the cracked segments. The cracked segments neighboring the image edges were not included in the calculations to not influence the measurements. With this approach, we systematically identified the dimensions of cracked "islands" in the image and thus obtained their statistical information. The analysis revealed [that] the segments are isotropic, as summarized in Figures 4.8 and 4.9, which figuratively summarize the analyses approach, showing a histogram of the cracked segment distributions. Adjacent to each histogram are the binarized images in which the blue "x" marks the centroid location of each cracked segment.

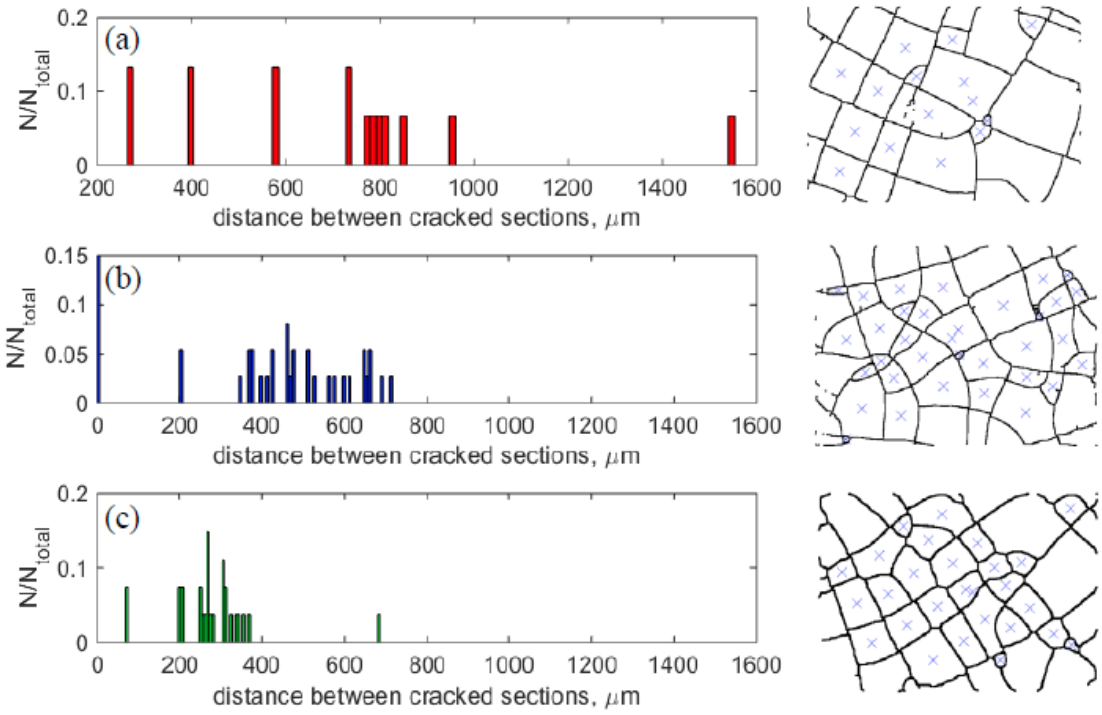

Figure 4.8: Overview of Cluster analysis for UV Treated Samples

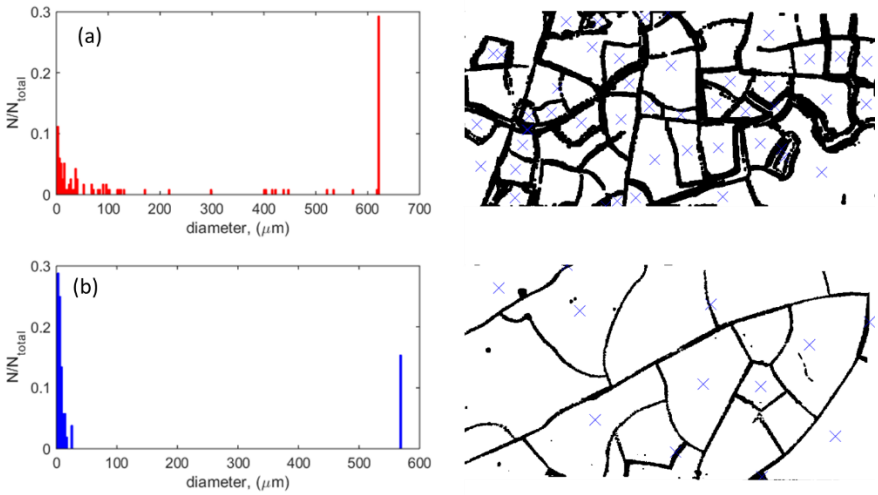

Figure 4.9: Overview of Cluster analysis for non-UV Treated Samples

We draw several conclusions from this cluster analysis. Beginning with the UV treated samples of Figure 4.8; the histograms show that as the substrate thickness decreases, the cluster segments become more isotropic with a narrower distribution. This is evidenced by the comparison between Figure 4.8(a), showing a sample with a PDMS thickness, $h_s = 50\mu m$, and 4.8(c) showing a sample with a PDMS thickness of $h_s = 6\mu m$. Although these observations may be unexpected, several observations could illuminate the cause: We note that the roughness of the PDMS samples after curing is within $10 - 16\%$ of the film thickness and the standard deviation of the roughness is much higher in the thicker samples. This and other observations are expanded on in Section 4.3.3

The samples that did not undergo UV treatment showed cracks similar to the UV treated samples but with a different average spacing. Figure 4.9 shows the crack network analysis of these Au-Si coatings, deposited on elastomer that did not undergo UV treatment. As highlighted in Section 2.4, the main motivation for the UV treatment is to enhance the interfacial adhesion and therefore reduce any delamination at the interface [58]. Based on this principle, the samples shown in Figure 4.9 that did not undergo UV treatment would be most susceptible to delamination. However, a FIB section view of that sample, shown in Figure 4.10, confirms that even though cracks did form, these cracks

penetrated into the substrate rather than deflecting along the interface, as would have been expected of a system with poor adhesion. This observation is one that needs to be understood.

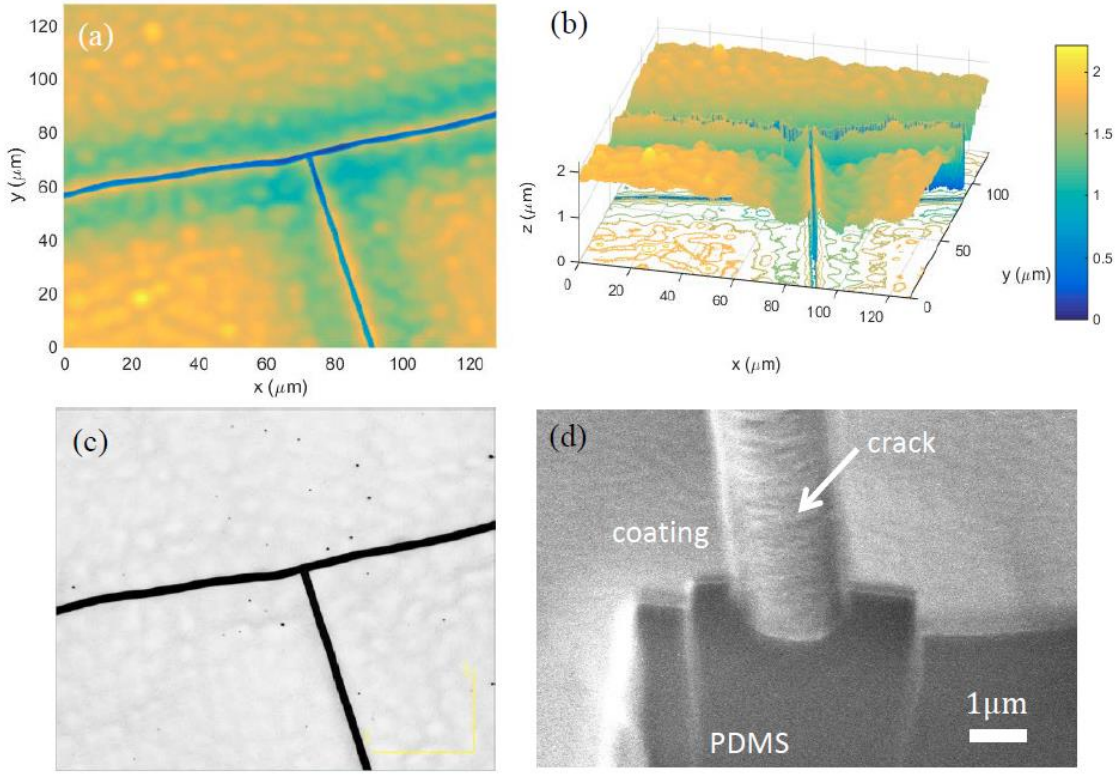

Figure 4.10: Examination of Cracks on non-UV Treated Bilayers

The summary of the crack segment statistics is shown in Figure 4.11. The raw data used to create the crack spacing plot was obtained from the cluster analysis while the crack opening displacement (COD) and crack data were obtained from confocal images. We observed from this data that crack depth and opening inversely scale with PDMS thickness while only crack depth has little dependence on UV treatment. In addition, the data in Figure 4.11(c) also confirm that cracks penetrated a few microns into the PDMS substrate thus exposing the elastomer to the free surface. Crack spacing also shows a dependence on PDMS thickness, as shown on Figure 4.11(a), with a threefold increase in the spacing over an order of magnitude increase in the PDMS thickness. We also observed that samples

prepared without the UV treatment step developed cracks distributed with a spacing three times greater than the spacing of the UV treated samples.

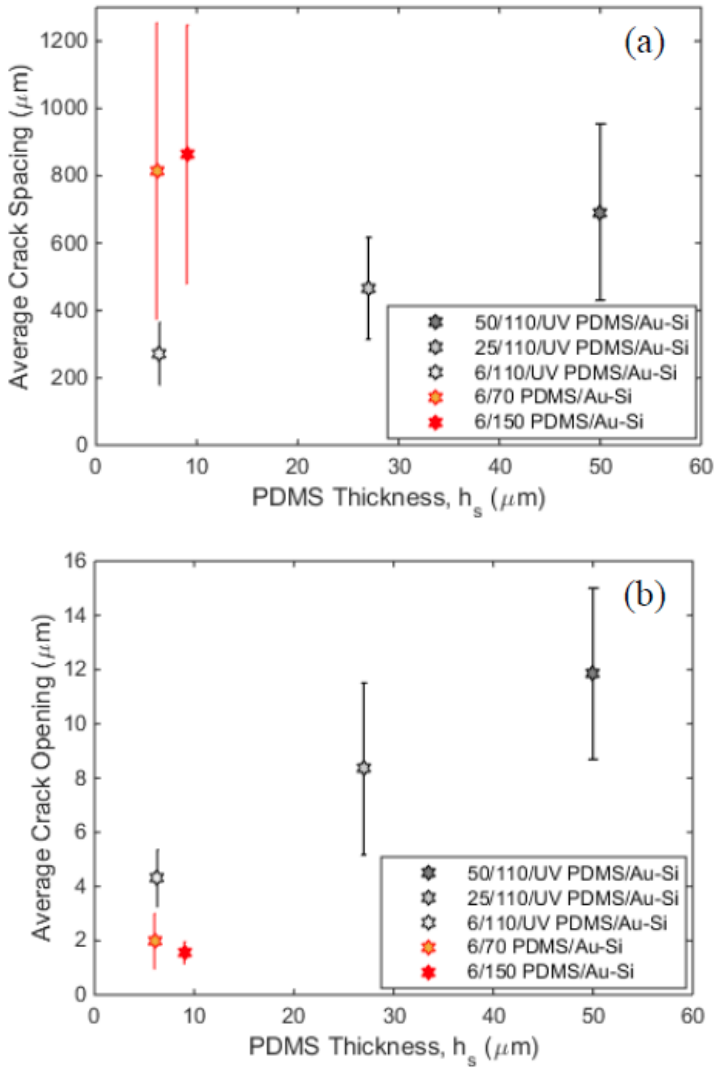

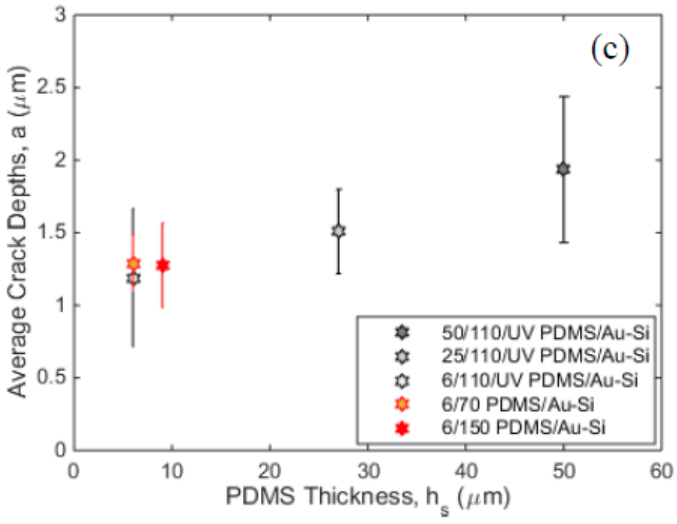

Figure 4.11: Summary of Crack analysis versus PDMS Thickness

4.3.3 Understanding the Experimental Observations

With the unexpected behaviors observed in the experimental analysis, we sought an explanation for the crucial factors at play. The experimental results show that UV treatment of the PDMS, as well as the PDMS thickness can have a profound effect on the types of patterns that can form on the coating surface after deposition is completed. The results suggest that a combination of both cracks and wrinkles can co-exist when a brittle coating (e.g. Au-Si) is deposited on a PDMS surface. The observed crack spacing and wrinkle wavelength in our experiments raise several questions that we expand on to draw conclusions on the mechanisms at work:

(1) *How could cracks form in samples where increasing levels of compressive mismatch strain have been introduced during deposition?*

Cracks form when a sufficiently high tensile stress exceeds the film fracture strength. But given that the thin film sputter parameters tuned to impose only compressive residual strains on the system, a condition confirmed by the presence of wrinkles in the UV treated ductile Au-Ag coating (these wrinkles indicates that during UV treatment the interfacial mismatch strains are still compressive), the

observation of tensile cracks is not expected. To explain why these cracks and wrinkles can co-exist without film delamination, we hypothesize that the cracks initiate at high stress regions of wrinkles. This was verified using a numerical model to examine the thin film stresses that develop. As a comparison, experimental observations of the mismatch strain levels from confocal microscopy are also presented. More details are presented in Section 4.3.4

(2) *Why does crack spacing appear to depend on PDMS thickness?*

This is a surprising observation since the PDMS samples are still rigidly attached on the glass substrate and the PDMS deposition surface should be stress free. However, from the roughness analysis presented earlier, it is apparent that the PDMS surfaces after curing have uneven surfaces or roughness with amplitudes that linearly scale with PDMS thickness, increasing from 10% of the film thickness for the lower thickness PDMS samples, to 16% for the samples with the largest thicknesses. The presence of the resulting rough interface following deposition may be an indication that the surface of the PDMS is not stress free after curing. We thus hypothesize that these variations result in the varying crack behavior.

(3) *Why was interfacial delamination not an issue in the samples regardless of UV treatment?*

UV treatment is similar to plasma treatment, its more damaging counterpart, in its potential to render an inherently hydrophobic PDMS surface temporarily hydrophilic. Therefore, as indicated previously, UV deposition is often performed on PDMS surfaces prior to deposition to create a strong interfacial bond that enhances interfacial adhesion [58, 80]. However, in addition to modifying the hydrophobicity of a PDMS substrate, studies have also reported that UV treatment alters the mechanical properties of the near surface PDMS (up to thicknesses $< 100nm$ below the surface) rendering it more stiff and brittle [34, 81, 82]. Although these effects of UV treatment, especially the improvement in adhesion because of

altered hydrophobicity, would make the UV treatment step a necessary step to create bilayers with strong adhesion, our results appear to suggest that a very strong interfacial bond forms after sputter deposition under bias, rendering the UV treatment step unnecessary. We note, concerning this observation, that depositions of hard films on substrates under bias have also shown strong interfacial adhesion and a very clean interface [83, 84].

4.4 Crack Initiation Model

To explain how cracks can initiate in a thin film under compressive mismatch strain and strong interfacial adhesion, we use a numerical model analyzed with two strain profiles that could capture some elements of the behavior. The model mainly focuses on examining how the PDMS properties could interact with mismatch strains to develop the wrinkles and cracks reported in the previous sub-section, so we simplified the model, within reason, to allow for FEM computation. The following sections outline the modelling steps and primary considerations made.

4.4.1 Geometry and Material Properties

Our FEM analysis utilizes a two-dimensional model with plane strain elements to ease computation. This approach is generally accepted for an analysis such as this because the primary dimension of concern is the through thickness. To ensure the veracity of FEM results, we designed the geometry of the model to match closely with experimental samples. However, this was complicated by the extreme aspect ratio of actual samples: The total length of samples, which were created on a glass slide, was several centimeters, whereas the thickness ranged between a few microns for the PDMS and 70nm for the coated film. Such high aspect-ratio models would be computationally expensive to perform, so we limit the length of our sample length based on the smallest crack spacing, which is $400\mu m$. In addition, by applying symmetry, we further reduced this dimension

to $200\mu m$. The thickness of the model is unchanged; however, the model neglects the glass substrate, on which the samples were prepared, and replaces it with a boundary constraint. This modification is invoked because the high stiffness and thickness of the glass slide would yield a negligible contribution to the overall model behavior. Figure 4.12 summarizes the geometrical model.

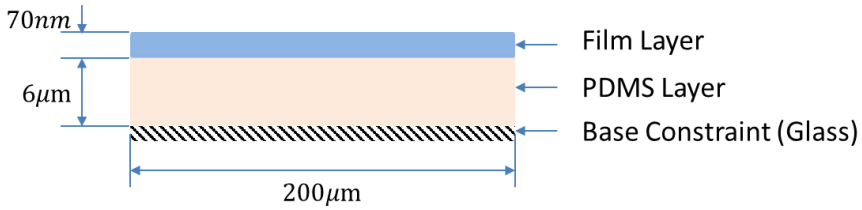

Figure 4.12: Schematic of Finite Element Model Geometry

Although the model maintains consistent geometry through all analyses, we vary the material properties to evaluate the effect of the modulus mismatch. Specifically, we adopt two moduli for the PDMS, $1MPa$ and $3MPa$, accounting for the temperature range, and vary the film modulus between $500MPa$ and $150GPa$.

4.4.2 Mesh Characteristics

Due to the high aspect ratio, a very fine mesh was required in order to avoid errors with the FEM analysis. In addition, we vary the height of the mesh through the PDMS thickness in order to account for the finer behavior at the interface while minimizing the number of elements incorporated into the model. Figure 4.13 shows a section of the meshed model.

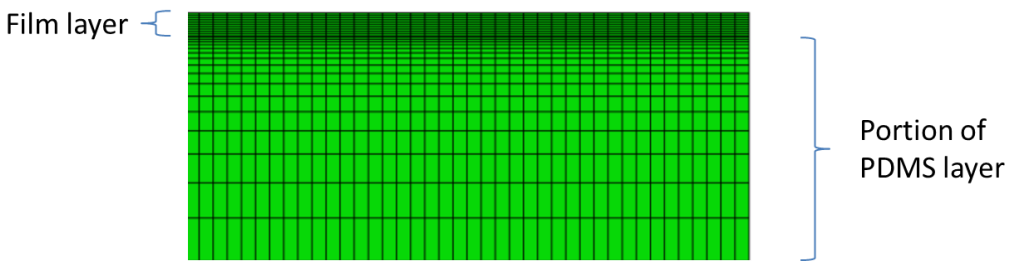

Figure 4.13: Section of Model Showing Mesh Characteristics

4.4.3 Loading and Boundary Conditions

As highlighted in the introduction to section 4.4, the primary goal of the model is to examine the role of PDMS properties and mismatch strains in generating wrinkles. Hence, to model the effect of the PDMS accurately, we must account for the modifications to the PDMS surface due to processing. To accomplish this, the model employs two mismatch strain profiles, as schematically shown in Figure 4.14(a). The first case, Case 1, shown in red in Figure 4.14(a), has a strain profile characterized by the following equation:

$$\varepsilon = \varepsilon_{\mathrm{M}} \left(\frac{2w}{W}\right) \tag{4.2}$$

This strain profile was applied at the interface between the PDMS and the thin film, that is, where $h = h_{\mathrm{f}}$. The term w in the expression refers to the lateral dimension, which ranges from zero to $W/2$, half the total lateral dimension of the sample. The second case, Case 2, shown in purple in Figure 4.14(a), is described by a strain profile of the following form:

$$\varepsilon = \varepsilon_{\mathrm{M}} \left(\frac{2w}{W}\right) e^{h_0(h-h_{\mathrm{s}})} \tag{4.3}$$

This profile was applied over a finite region of the PDMS close to the interface, where the position along the thickness $h \geq h_{\mathrm{f}}$. In this expression, h is the through thickness dimension, and h_0 is the penetration depth, or the depth that the mismatch strain infiltrates into the substrate. As such, if $h_0 = 100$, then the mismatch strain profile rapidly decays within the span of ~100nm.

In addition, y-constraint boundary conditions were applied at the base of the model with a rotation constraint at the left corner of the model. Figure 4.14(c) shows these loading and boundary conditions on the model as viewed in the FEM software, Abaqus.

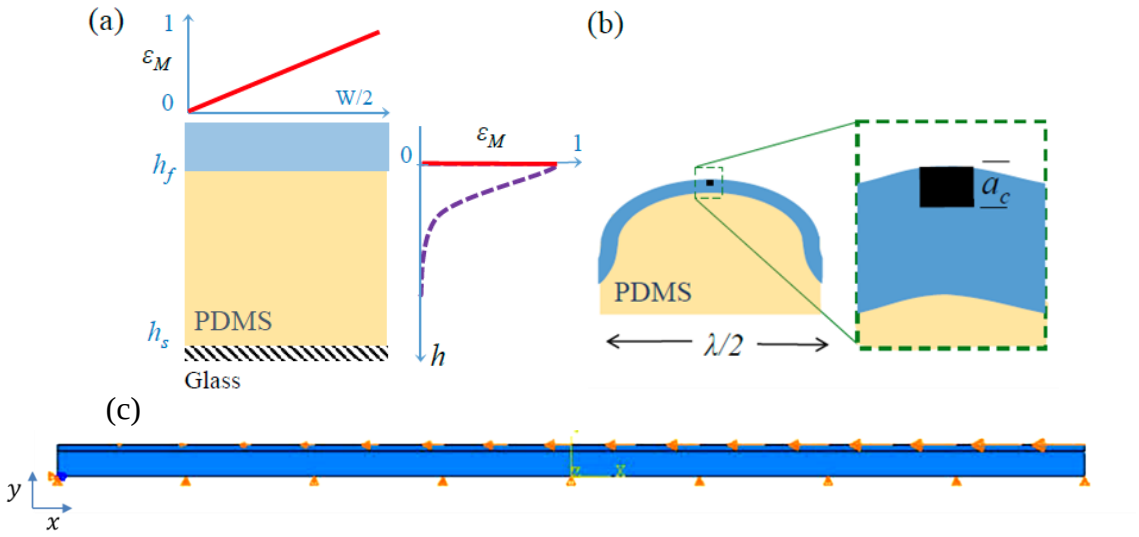

Figure 4.14: Schematic of Strain Model

The two profile models used were adopted to reflect the experimental conditions. The rationale for employing Case 2 was to examine whether mismatch strains, distributed through a finite depth of the PDMS, could account for some of the observations. These mismatch strains that we model may originate in the experimental samples during the UV treatment and/or sputter deposition step itself, either by heating/cooling of the substrate, or through ion bombardment and other similar processes that may lead to modification of the near surface properties of the elastomer. The penetration depth accounts for surface modification due to these processing conditions, which could affect the PDMS to varying depths, depending on condition used. For both Case 1 and Case 2, however, the maximum mismatch strain will develop at the interface. In our FEM model, we applied a mismatch strain up to $\varepsilon_{\mathrm{M}} = 1\%$. This resulted in surface wrinkle formation, the profile of which is shown in Figure 4.15, for both strain profile cases. In both models, two substrate moduli were used: $E_{\mathrm{s}} = 1\mathrm{MPa}$ and $E_{\mathrm{s}} = 3\mathrm{MPa}$. In addition, for Case 2, two depth profiles were examined: $h_0 = 50$ and $h_0 = 100$.

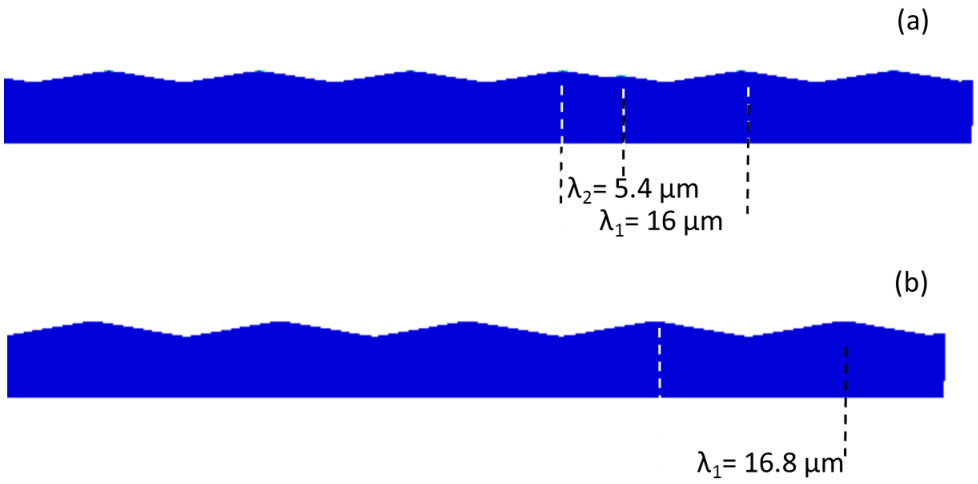

Figure 4.15: Profile of Generated Wrinkles from FEM Model

4.4.4 FEM Model Results

The finite element models revealed much. Upon examining the principal stresses that developed at the wrinkle peak of Figure 4.15(b), we found that the in plane maximum principal stress is non-uniform through the film thickness. The (tensile) stress distribution involved a peak that occurred at the top of the wrinkle along with a rapid decrease in stress within 30% of the film thickness. This distribution is plot in Figure 4.16, which shows the in-plane principal stress at the peak of a wrinkle. The non-uniform stress profile leads to a bending stress that causes tensile stress to develop at the top surface of the thin film. With this tensile stress present in the film, cracks will initiate at the peak of the wrinkles, where the tensile stresses are at a maximum. This crack initiation occurs when the principal tensile stress at these peaks exceeds a critical fracture stress, which can be calculated by applying fracture mechanics principles, following Equation 4.4 [85]:

$$K_{\mathrm{I}} = \sigma_b \sqrt{\pi a} F\left(\frac{a}{h_{\mathrm{f}}}\right) Z(\alpha, \beta) \tag{4.4}$$

σ_{b}, in this expression, is the bending stress, a is the crack size, and $F(a/h_{\mathrm{f}})$ is a geometrical factor dependent on the ratio of the crack size to the film thickness, h_{f}. Since the high tensile stresses are confined within $0.3h_{\mathrm{f}}$, as for instance is the case for a shallow crack, so

that $F(0.3)\sim0.7$ [86]. The parameter, $Z(\alpha,\beta)$, is a constraint factor, dependent on the Dundurs' parameters. This factor is obtained experimentally and has been explored for films subject to uniform tensile stresses [87, 88].

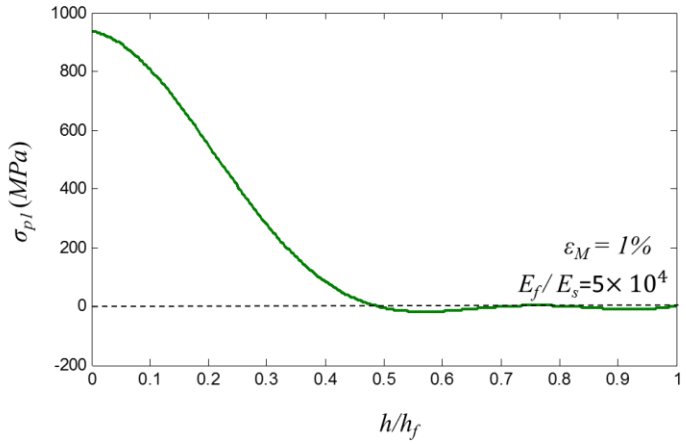

Figure 4.16: Stress Distribution at Wrinkle Peak versus Normalized Thickness

For the bilayers in this study, with Dundurs' parameter values of $\alpha \cong 1$ and $\beta \cong 0.25$, the constraint factor yields a value of $Z(1,0.25)\sim35$. Studies have shown that this constraint value, generally associated with films deposited on very compliant substrates, entails a very large crack driving force that causes cracks to initiate more readily. The failure stress associated with this driving force can be calculated by equating the driving force with the fracture toughness ($K_{\mathrm{I}} = K_{\mathrm{Ic}}$), so that

$$\sigma_{\mathrm{bf}} = \left(\frac{K_{\mathrm{Ic}}}{Z}\right)/(0.7\sqrt{\pi a}) \tag{4.5}$$

The predictions of this model for Case 1 and Case 2 and parameters (E_{s}, h_0) are summarized in Figure 4.17. In this figure, the maximum in-plane principal tensile stress in the thin film is normalized relative to the product of the film modulus and the maximum imposed compressive mismatch strain ($\varepsilon_{\mathrm{M}}^{max} = 1\%$) and presented as a function of the imposed mismatch strain. The horizontal lines show the failure stress σ_{bf} from Equation 4.5, normalized with the film modulus and the maximum imposed compressive mismatch

strain. These horizontal lines were generated for a critical crack size of $a_c = 0.2h_f$. Each line corresponds to a distinct K_{Ic}/Z ratio.

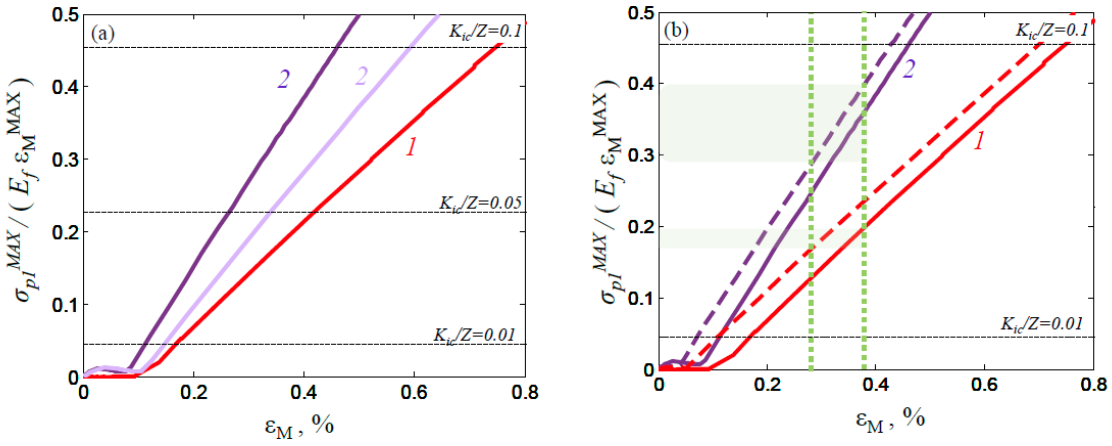

Figure 4.17: Summary of Stress versus Strain Behavior from Model

As can be observed in Figure 4.17, the properties appear to play a role in the stress condition. Since the fracture toughness of the film used isn't clear, we assume a fracture toughness of Au-Si close to that of silicon (Si) ($\sim 1\text{MPa}\sqrt{\text{m}}$) [89], which is the weaker material in the alloy. Figure 4.17(a) characterizes the bilayers with PDMS (substrate) moduli of $E_s = 3\text{MPa}$. The red line in the figure shows the results of Case 1, with a concentrated mismatch strain following Equation 4.2. The purple lines show the results of Case 2, following Equation 4.3, for two mismatch strain penetration depths: $h_0 = 50$ (light purple) and $h_0 = 100$ (dark purple). These purple curves show the effect of penetration depth on the stress state of the bilayer: The deeper the mismatch strain profile in the elastomer, the lower the level of imposed mismatch strain is needed to initiate both wrinkles and cracks. For example, if the critical fracture stress occurs when $K_{Ic}/Z = 0.05$, then an imposed mismatch strain of just 0.27% would be needed to initiate both wrinkles and cracks in a profile similar to Case 2 whereas a 60% higher level of mismatch strain would be needed to initiate wrinkle and cracks in a system with a concentrated mismatch strain profile of Case 1.

Based on the results of Figure 4.17, one could conclude that, if any surface modification procedures do introduce mismatch strains into the elastomer, very low levels of mismatch strain would be needed to initiate cracks, even if interfacial delamination is avoided. Curiously, Case 2 exhibited nested wrinkles of two wavelengths, $\lambda_1 \sim 14\mu m$ and $\lambda_2 \sim 5\mu m$. We observed that the smaller wavelength wrinkles did not have as high levels of tensile stress on their top surface as the larger wavelengths. Furthermore, in the systems with a higher concentration of the mismatch strain at the interface, we observed a single wavelength. For the models that did not show a single wavelength, the wavelengths of the nested wrinkles are shown in Figure 4.5, along with the experimental observations. These results show that the nested wrinkle profile from the model is within the same range as the experimentally observed nested wrinkles, suggesting that the model does capture some of the key physics of the complex sputter-deposition process. This could also indicate that the nested wrinkles are highly dependent on the profile of the imposed mismatch strain. In light of this, it may be possible for one to tune fabrication of other surface features such as folds or creases without merely increasing the mismatch strain magnitude but by tuning the profile and depth of the mismatch strain through such techniques as sputter deposition.

More information on the model is presented in Figure 4.17(b), which shows the results for the concentrated mismatch strain of Case 1 (red lines), and the largest penetration depth, Case 2a (purple lines), for separate substrate moduli. The dotted red and purple lines correspond to the results when the substrate modulus was modelled at $E_s = 1\text{MPa}$ while the solid red or purple lines correspond to $E_s = 3\text{MPa}$. These two moduli were explored because experimental measurements were made for PDMS cured at two temperatures, resulting in bilayers with distinct substrate moduli values. The two moduli used reflect the difference that results from the curing temperatures. The green vertical dotted lines correspond to the experimental observations of the mismatch strain measured from the confocal microscopy, as summarized in Figure 4.17.

The model successfully reproduced several other experimental observations. A crucial behavior that it captures is the dependence of mismatch strains on substrate modulus. The model shows that a difference in the substrate modulus can lead to a difference in the mismatch strains; with a more compliant substrate initiating wrinkles and cracks when 20% lower mismatch strain is applied. Figure 4.17(b) conveys this: The shaded green region of the figure for Case 1 mismatch strain profile. The experimental results suggest that $K_{Ic}/Z \sim 0.04$ whereas the Case *2* results suggest a larger spread that $0.06 < K_{Ic}/Z < 0.09$. In both cases, assuming $K_{Ic} = 1MPa\sqrt{m}$, the constraint factor is $Z \sim 25$ for Case 1. On the other hand, if the mismatch strain profile is similar to Case2 then the constraint factor can be much lower $11 < Z < 16$. The simple captures crucial features observed in the experiment, namely the appearance of nested wrinkles with a good comparison of their wavelength. It can be helpful in demonstrating how cracks may initiate when very high tensile stresses at the top of wrinkles exceed the critical fracture stress for a brittle thin film.

4.5 Summary and Conclusions

In summary, the study presented in this chapter probed the surface patterns generated when a thin coating with a large modulus mismatch was sputter deposited onto an elastomer. In particular, we explore the concurrent formation of wrinkles and cracks, which was not expected for samples deposited under compressive mismatch stresses and strong interfacial adhesion. To explain this phenomenon, we presented a rationale for the formation of the cracks while examining the effect of curing parameters, substrate thickness and UV treatment on the eventual surface topology of sputtered brittle and ductile coatings. The main findings are listed as follows:

1. Both nested wrinkles and cracks appear on the surface of non-UV treated brittle coatings of Au-Si. However, only cracks appear on UV-treated Au-Si films and only wrinkles appear on ductile Au-Ag films.

2. The wrinkle wavelength measured is in good agreement with theoretical predictions for the Au-Ag films. In addition, the nested wrinkle dimensions are not captured by any existing model unless a very large mismatch strain at the interface is applied.
3. Residual compressive stresses develop in the film because of the sputter deposition. However, the cracks that appear on the surface are not formed from delamination at the interface as verified from confocal images and a focused ion beam SEM cross-section view.
4. Crack characteristics showed dependence on several factors: Crack spacing is a factor of four smaller if PDMS is UV-treated and a factor of three smaller as the elastomer thickness decreases from 30 to 6μm. Crack-tip opening displacement is 2 times larger if PDMS is UV treated and 3 times smaller if elastomer thickness decreases from 30 to 6μm. The crack depth is invariant with the UV treatment and always penetrates through the film and elastomer. The depth decreases by a factor of two as the elastomer thickness changes from 30 to 6μm. These observations show dependence of the crack characteristics with the substrate properties, which is not expected.
5. A finite element model investigated the wrinkle wavelength and tensile stresses that develop in the thin film after application of mismatch strain at the interface or through a finite depth in the elastomer. This model revealed that large tensile stresses can develop at the peak of the wrinkles and that nested wrinkles can form in the case where the mismatch strain penetrates thorough a finite depth of the elastomer. In such a case, mismatch strains at the interface can be less than 1% to initiate nested wrinkles. The constraint imposed from the elastomer can decrease the fracture strength needed to initiate cracks.

In conclusion, the work in this chapter demonstrated formation of concurrent cracks and nested wrinkles on the surface of sputtered films on very compliant substrates. The cracks

are not a result of delamination at the interface but are thought to originate from the peak of wrinkles when a critical fracture stress is achieved. The simple model can be used to design surface instabilities by modulating factors such as the fracture toughness and the constraint of the substrate. The results also suggest that UV treatment is not necessary in enhancing interfacial adhesion when thin films are deposited by sputtering. Additional experiments could provide further understanding of how the mismatch strain profile can be tuned by altering the sputter deposition parameters to generate complex surface patterns such as folds on the surface without generating cracks and by eliminating a step in the fabrication process.

CHAPTER 5

CLOSING REMARKS AND SUGGESTIONS FOR FUTURE WORK

5.1 Future Work

As mentioned in the introduction section, the main study of this thesis is motivated by a broader goal of creating bilayers of a nanoporous (NP) metal and an elastomer. The previous chapters have focused on an intermediate, but necessary step of building an understanding of possible failure or instability conditions due to fabrication decisions. The next step of this project, therefore, will be to perfect the technique of creating nanoporous polymer-metallic bilayers that can undergo actuation. In this regard, three major tasks need are essential:

i. *Creating nanoporous metal by dealloying bilayers*: This requires an understanding of the proper dealloying conditions that can be adopted without causing delamination of the nanoporous film from the substrate.

ii. *Dealloying in the presence of cracks*: Cracks tend to disrupt charge flow and hence hinder the dealloying process. For some bilayer conditions, these cracks are unavoidable. Thus, in order to create nanoporous foams on these cracked surfaces, a suitable method needs to be developed to bridge the disconnects created by cracks and allow for dealloying to proceed smoothly.

iii. *Machining and release of dealloyed bilayers*: Once the process of creating the nanoporous layer is perfected, sections of these bilayers, small enough to actuate without the hindering effects of weight and similar factors, need to be created without damaging the nanoporous layer.

Efforts were made to accomplish these tasks; however, insufficient data is currently available to report. Although complete control has not been established, preliminary attempts were made to dealloy elastomer-metal alloy bilayers. The dealloying process was

attempted on bilayers of Cu-Si and PDMS. Some samples yielded a porous metal; these were the subject of the analysis presented in this section. SEM images of the resulting foam are shown in Figure 5.3. The results show the feasibility of developed approaches to creating the desired bilayers.

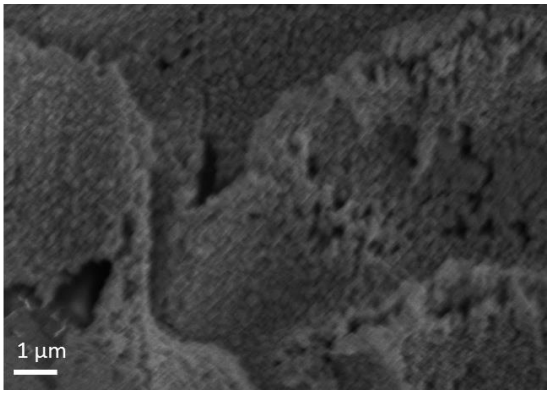

Figure 5.1: SEM of Generated Foam

5.2 Concluding Remarks

In conclusion, this thesis has discussed the challenge of creating bilayers with very high-property mismatch. The previous sections show a few of the many research paths that could follow-up from this study. Although much is still unclear regarding the topic discussed, the information presented herein could serve as a good foundation for future study.

REFERENCES

1. Breid, D. and A.J. Crosby, *Effect of stress state on wrinkle morphology*. Soft Matter, 2011. **7**(9): p. 4490-4496.
2. Jiang, H., et al., *Finite deformation mechanics in buckled thin films on compliant supports.* Proceedings of the National Academy of Sciences, 2007. **104**(40): p. 15607-15612.
3. Efimenko, K., et al., *Nested self-similar wrinkling patterns in skins.* Nature materials, 2005. **4**(4): p. 293-297.
4. Chan, E.P., et al., *Surface wrinkles for smart adhesion.* Advanced Materials, 2008. **20**(4): p. 711-716.
5. Jambon-Puillet, E., D. Vella, and S. Protiere, *The compression of a heavy floating elastic film.* Soft Matter, 2016.
6. Freund, L.B. and S. Suresh, *Thin film materials: stress, defect formation and surface evolution*. 2004: Cambridge University Press.
7. Suhir, E., *Interfacial stresses in bimetal thermostats.* Journal of Applied mechanics, 1989. **56**(3): p. 595-600.
8. Hsueh, C.H., C.R. Luttrell, and T. Cui, *Thermal stress analyses of multilayered films on substrates and cantilever beams for micro sensors and actuators.* Journal of Micromechanics and Microengineering, 2006. **16**(11): p. 2509.
9. Olsen, G. and M. Ettenberg, *Calculated stresses in multilayered heteroepitaxial structures.* Journal of Applied Physics, 1977. **48**(6): p. 2543-2547.
10. Dauskardt, R., et al., *Adhesion and debonding of multi-layer thin film structures.* Engineering Fracture Mechanics, 1998. **61**(1): p. 141-162.
11. Charles, L.H., *Bimetal strip thermostat*. 1952, Google Patents.
12. Clark, A.E., M. Wun-Fogle, and J.B. Restorff, *Bimetallic Strips for Energy Harvesting, Actuation and Sensing*. 2010, Google Patents.
13. Huang, M.H., et al., *Nanomechanical architecture of strained bilayer thin films: From design principles to experimental fabrication.* Advanced Materials, 2005. **17**(23): p. 2860-+.
14. Prinz, V.Y., et al., *Nanoscale engineering using controllable formation of ultra-thin cracks in heterostructures.* Microelectronic Engineering, 1996. **30**(1-4): p. 439-442.
15. Schmidt, O.G. and K. Eberl, *Nanotechnology - Thin solid films roll up into nanotubes.* Nature, 2001. **410**(6825): p. 168-168.
16. Yablonovitch, E., et al., *EXTREME SELECTIVITY IN THE LIFT-OFF OF EPITAXIAL GAAS FILMS.* Applied Physics Letters, 1987. **51**(26): p. 2222-2224.
17. Huang, S.S. and X. Zhang, *Gradient residual stress induced elastic deformation of multilayer MEMS structures.* Sensors and Actuators a-Physical, 2007. **134**(1): p. 177-185.
18. Yu, S., et al., *Wrinkled stripes localized by cracks in metal films deposited on soft substrates.* Soft matter, 2015. **11**(11): p. 2203-2212.
19. Dundurs, J., *Discussion: "Edge-Bonded Dissimilar Orthogonal Elastic Wedges Under Normal and Shear Loading" (Bogy, D. B., 1968, ASME J. Appl. Mech., 35, pp. 460–466).* Journal of Applied Mechanics, 1969. **36**(3): p. 650-652.

20. Kalaitzidou, K. and A.J. Crosby, *Adaptive polymer particles.* Applied Physics Letters, 2008. **93**(4): p. 041910.
21. Simpson, B., et al., *Capture/release ability of thermo-responsive polymer particles.* Journal of Materials Chemistry, 2010. **20**(17): p. 3496-3501.
22. Dai, M., et al., *Humidity-Responsive Bilayer Actuators Based on a Liquid-Crystalline Polymer Network.* ACS Applied Materials & Interfaces, 2013. **5**(11): p. 4945-4950.
23. Randhawa, J.S., et al., *Microchemomechanical Systems.* Advanced Functional Materials, 2011. **21**(13): p. 2395-2410.
24. Santos, P.A., et al., *Polyamide-6/vegetal fiber composite prepared by extrusion and injection molding.* Composites Part A: Applied Science and Manufacturing, 2007. **38**(12): p. 2404-2411.
25. Bourbigot, S., et al., *PA-6 clay nanocomposite hybrid as char forming agent in intumescent formulations.* Fire and Materials, 2000. **24**(4): p. 201-208.
26. Stoychev, G., et al., *Shape-Programmed Folding of Stimuli-Responsive Polymer Bilayers.* ACS Nano, 2012. **6**(5): p. 3925-3934.
27. Lixin, D., et al., *Nanorobotics for creating NEMS from 3D helical nanostructures.* Journal of Physics: Conference Series, 2007. **61**(1): p. 257.
28. Armani, D., C. Liu, and N. Aluru. *Re-configurable fluid circuits by PDMS elastomer micromachining*. in *Technical Digest. IEEE International MEMS 99 Conference. Twelfth IEEE International Conference on Micro Electro Mechanical Systems (Cat. No.99CH36291)*. Place of Publication: Piscataway, NJ, USA; Orlando, FL, USA. Country of Publication: USA.: IEEE IEEE Robotics & Autom. Soc IEEE Robotics & Autom. Soc.
29. Zhang, Y., et al., *A mechanically driven form of Kirigami as a route to 3D mesostructures in micro/nanomembranes.* Proceedings of the National Academy of Sciences, 2015. **112**(38): p. 11757-11764.
30. Kim, B.C., et al., *Guided fracture of films on soft substrates to create micro/nano-feature arrays with controlled periodicity.* Scientific Reports, 2013. **3**: p. 3027.
31. Seghir, R. and S. Arscott, *Controlled mud-crack patterning and self-organized cracking of polydimethylsiloxane elastomer surfaces.* Scientific reports, 2015. **5**.
32. Huh, D., et al., *Tuneable elastomeric nanochannels for nanofluidic manipulation.* Nat Mater, 2007. **6**(6): p. 424-428.
33. Mills, K.L., et al., *Instantaneous fabrication of arrays of normally closed, adjustable, and reversible nanochannels by tunnel cracking.* Lab on a Chip, 2010. **10**(12): p. 1627-1630.
34. Zhou, J., A.V. Ellis, and N.H. Voelcker, *Recent developments in PDMS surface modification for microfluidic devices.* ELECTROPHORESIS, 2010. **31**(1): p. 2-16.
35. Wang, Q. and X. Zhao, *A three-dimensional phase diagram of growth-induced surface instabilities.* Scientific reports, 2015. **5**.
36. Schmauder, S. and M. Meyer, *Correlation between Dundurs' parameters and elastic constants.* Z. Metallkd, 1992. **83**(7): p. 525.
37. Neuber, H., *NI Muskhelishvili, Some basic problems of the mathematical theory of elasticity. 3. verb. und vermehrte Auflage.(Aus dem Russischen übersetzt von JRM Radok.) XXXI+ 704 S. m. 66 Abb. Groonigen (Holl.) 1953. Verlag P.*

Noordhoff Ltd. Preis geb. 38.–fl. ZAMM-Journal of Applied Mathematics and Mechanics/Zeitschrift für Angewandte Mathematik und Mechanik, 1954. **34**(12): p. 479-479.
38. Antoniou, A., et al., *Controlled nanoporous Pt morphologies by varying deposition parameters.* Applied Physics Letters, 2009. **95**(7): p. 073116.
39. Liu, R. and A. Antoniou, *A relationship between the geometrical structure of a nanoporous metal foam and its modulus.* Acta Materialia, 2013. **61**(7): p. 2390-2402.
40. Ashby, M.F., *Materials selection in mechanical design*. 4th ed. ed. 2011, Butterworth-Heinemann: Burlington, MA.
41. Detsi, E., et al., *Actuating and sensing properties of nanoporous gold.* Journal of nanoscience and nanotechnology, 2012. **12**(6): p. 4951-4955.
42. Ouyang, G., et al., *Nanoporous Structures: Smaller is Stronger.* Small, 2008. **4**(9): p. 1359-1362.
43. Fujita, T., et al., *Atomic origins of the high catalytic activity of nanoporous gold.* Nat Mater, 2012. **11**(9): p. 775-780.
44. Kraehnert, R., et al., *Electrochemically dealloyed platinum with hierarchical pore structure as highly active catalytic coating.* Catalysis Science & Technology, 2015. **5**(1): p. 206-216.
45. Biener, J., et al., *Surface-chemistry-driven actuation in nanoporous gold.* Nature materials, 2009. **8**(1): p. 47-51.
46. Detsi, E., P. Onck, and J.T.M. De Hosson, *Metallic Muscles at Work: High Rate Actuation in Nanoporous Gold/Polyaniline Composites.* ACS Nano, 2013. **7**(5): p. 4299-4306.
47. Brett, C., et al., *Electrochemistry: principles, methods, and applications*. 1993.
48. Brett, C.M.A. and A.M. Oliveira Brett, *Electrochemistry - Principles, Methods, and Applications*. Oxford University Press.
49. Bard, A.J., R. Parsons, and J. Jordan, *Standard potentials in aqueous solution*. Vol. 6. 1985: CRC press.
50. Mark, J.E., *89. Poly(dimethylsiloxane)*, in *Polymer Data Handbook (2nd Edition)*. Oxford University Press.
51. Palchesko, R.N., et al., *Development of Polydimethylsiloxane Substrates with Tunable Elastic Modulus to Study Cell Mechanobiology in Muscle and Nerve.* PLoS ONE, 2012. **7**(12): p. e51499.
52. Kelly, P.J. and R.D. Arnell, *Magnetron sputtering: a review of recent developments and applications.* Vacuum, 2000. **56**(3): p. 159-172.
53. Thornton, J.A., *Magnetron sputtering: basic physics and application to cylindrical magnetrons.* Journal of Vacuum Science & Technology, 1978. **15**(2): p. 171-177.
54. Swann, S., *Magnetron sputtering.* Physics in Technology, 1988. **19**(2): p. 67.
55. Parsons, R., *Sputter deposition processes.* Thin film processes II, 1991: p. 177-208.
56. Vossen, J.L. and W. Kern, *Thin Film Processes II*. Elsevier.
57. Vig, J.R., *UV/ozone cleaning of surfaces.* Journal of Vacuum Science & Technology A, 1985. **3**(3): p. 1027-1034.

58. Mathieson, I. and R. Bradley, *Improved adhesion to polymers by UV/ozone surface oxidation.* International Journal of Adhesion and Adhesives, 1996. **16**(1): p. 29-31.
59. Mathieson, I. and R. Bradley, *Surface oxidation of poly ether ether ketone films using ultraviolet/ozone.* Journal of Materials Chemistry, 1994. **4**(7): p. 1157-1157.
60. Kelly, R., *Thermal effects in sputtering.* Surface Science, 1979. **90**(2): p. 280-318.
61. Freund, L.B., *Thin film materials : stress, defect formation, and surface evolution*, ed. S. Suresh. 2003, Cambridge University Press: Cambridge, England ;.
62. Casper, M.D., et al., *Surface wrinkling by chemical modification of poly(dimethylsiloxane)-based networks during sputtering.* Soft Matter, 2013. **9**(32): p. 7797-7803.
63. Chung, J.Y., J.P. Youngblood, and C.M. Stafford, *Anisotropic wetting on tunable micro-wrinkled surfaces.* Soft Matter, 2007. **3**(9): p. 1163-1169.
64. Herminghaus, S., M. Brinkmann, and R. Seemann, *Wetting and Dewetting of Complex Surface Geometries.* Annual Review of Materials Research, 2008. **38**(1): p. 101-121.
65. Quéré, D., *Wetting and Roughness.* Annual Review of Materials Research, 2008. **38**(1): p. 71-99.
66. Khare, K., J. Zhou, and S. Yang, *Tunable Open-Channel Microfluidics on Soft Poly(dimethylsiloxane) (PDMS) Substrates with Sinusoidal Grooves.* Langmuir, 2009. **25**(21): p. 12794-12799.
67. Watanabe, M., H. Shirai, and T. Hirai, *Wrinkled polypyrrole electrode for electroactive polymer actuators.* Journal of Applied Physics, 2002. **92**(8): p. 4631-4637.
68. Kim, J.B., et al., *Wrinkles and deep folds as photonic structures in photovoltaics.* Nat Photon, 2012. **6**(5): p. 327-332.
69. Hutchinson, J.W. and Z. Suo, *Mixed mode cracking in layered materials.* Advances in applied mechanics, 1991. **29**: p. 63-191.
70. Ebata, Y., A.B. Croll, and A.J. Crosby, *Wrinkling and strain localizations in polymer thin films.* Soft Matter, 2012. **8**(35): p. 9086-9091.
71. Li, B., et al., *Mechanics of morphological instabilities and surface wrinkling in soft materials: a review.* Soft Matter, 2012. **8**(21): p. 5728-5745.
72. Kim, P., M. Abkarian, and H.A. Stone, *Hierarchical folding of elastic membranes under biaxial compressive stress.* Nature materials, 2011. **10**(12): p. 952-957.
73. Thouless, M.D., et al., *Periodic cracking of films supported on compliant substrates.* Journal of the Mechanics and Physics of Solids, 2011. **59**(9): p. 1927-1937.
74. Johnston, I.D., et al., *Mechanical characterization of bulk Sylgard 184 for microfluidics and microengineering.* Journal of Micromechanics and Microengineering, 2014. **24**(3): p. 035017.
75. Liu, R., et al., *Synthesis and mechanical behavior of nanoporous nanotwinned copper.* Applied Physics Letters, 2013. **103**(24): p. 241907.
76. Gupta, G., et al., *Fluid and Resistive Tethered Lipid Membranes on Nanoporous Substrates.* The Journal of Physical Chemistry B, 2015. **119**(40): p. 12868-12876.
77. Abràmoff, M.D., P.J. Magalhães, and S.J. Ram, *Image processing with ImageJ.* Biophotonics international, 2004. **11**(7): p. 36-42.

78. Efimenko, K., et al., *Nested self-similar wrinkling patterns in skins.* Nat Mater, 2005. **4**(4): p. 293-297.
79. Jiang, H., et al., *Finite deformation mechanics in buckled thin films on compliant supports.* Proceedings of the National Academy of Sciences of the United States of America, 2007. **104**(40): p. 15607-15612.
80. Fu, Y.-J., et al., *Effect of UV-Ozone Treatment on Poly(dimethylsiloxane) Membranes: Surface Characterization and Gas Separation Performance.* Langmuir, 2010. **26**(6): p. 4392-4399.
81. Özçam, A.E., K. Efimenko, and J. Genzer, *Effect of ultraviolet/ozone treatment on the surface and bulk properties of poly(dimethyl siloxane) and poly(vinylmethyl siloxane) networks.* Polymer, 2014. **55**(14): p. 3107-3119.
82. Efimenko, K., W.E. Wallace, and J. Genzer, *Surface Modification of Sylgard-184 Poly(dimethyl siloxane) Networks by Ultraviolet and Ultraviolet/Ozone Treatment.* Journal of Colloid and Interface Science, 2002. **254**(2): p. 306-315.
83. Laing, K., et al., *The effect of ion current density on the adhesion and structure of coatings deposited by magnetron sputter ion plating.* Surface and Coatings Technology, 1999. **112**(1–3): p. 177-180.
84. Pan, A. and J.E. Greene, *Interfacial chemistry effects on the adhesion of sputter-deposited TiC films to steel substrates.* Thin Solid Films, 1982. **97**(1): p. 79-89.
85. Roylance, D., *Introduction to fracture mechanics.* 2001.
86. Dowling, N.E., *Mechanical behavior of materials: engineering methods for deformation, fracture, and fatigue*. 1993: Prentice hall.
87. Beuth Jr, J.L., *Cracking of thin bonded films in residual tension.* International Journal of Solids and Structures, 1992. **29**(13): p. 1657-1675.
88. Huang, R., et al., *Channel-cracking of thin films with the extended finite element method.* Engineering Fracture Mechanics, 2003. **70**(18): p. 2513-2526.
89. Ericson, F., S. Johansson, and J.-Å. Schweitz, *Hardness and fracture toughness of semiconducting materials studied by indentation and erosion techniques.* Materials Science and Engineering: A, 1988. **105**: p. 131-141.